PHYSICAL REVIEW E **100**, 013104 (2019)

# Effect of chordwise wing flexibility on flapping flight of a butterfly model using immersed-boundary lattice Boltzmann simulations

Kosuke Suzuki[*]
*Institute of Engineering, Academic Assembly, Shinshu University, Nagano 380-8553, Japan*

Takaaki Aoki[†]
*Department of Engineering, Graduate School of Science and Technology, Shinshu University, Nagano 380-8553, Japan*

Masato Yoshino[‡]
*Institute of Engineering, Academic Assembly, Shinshu University, Nagano 380-8553, Japan*

(Received 14 January 2019; published 11 July 2019)

Wing flexibility is one of the important factors not only for lift and thrust generation and enhancement in flapping flight but also for development of micro-air vehicles with flapping wings. In this study, we construct a flexible wing with chordwise flexibility by connecting two rigid plates with a torsion spring, and investigate the effect of chordwise wing flexibility on the flapping flight of a simple butterfly model by using an immersed boundary-lattice Boltzmann method. First, we investigate the effects of the spring stiffness on the aerodynamic performance when the body of the model is fixed. We find that the time-averaged lift and thrust forces and the required power increase with the spring stiffness. In addition, we find an appropriate range of the spring stiffness where the time-averaged lift and thrust forces are larger than those of the rigid wings. The mechanism of the lift and thrust enhancements is as follows: in the downstroke the flexible wings can generate not only the lift force but also the thrust force due to the deformation of wings; in the upstroke the flexible wings can generate not only the thrust force but also the lift force due to the deformation of wings. Second, we simulate free flights when the body of the model can only move translationally. We find that the model with the flexible wings at an appropriate value of the spring stiffness can fly more effectively than the model with the rigid wings, which is consistent with the results when the body of the model is fixed. Finally, we simulate free flights with pitching rotation. We find that the model gets off balance for any value of the spring stiffness. Therefore, the passive control of the pitching motion by the chordwise wing flexibility cannot be expected for the present butterfly model.

DOI: 10.1103/PhysRevE.100.013104

## I. INTRODUCTION

Insects fly freely in the air. The flight of insects propelled by flapping is an interesting phenomenon not only in biology but also in aerodynamics. In addition, its practical use for the development of micro-air vehicles (MAVs) has recently attracted a lot of attention [1]. Actually, the free flight of an insect-scale flapping-wing robot modeled loosely on the morphology of flies (a robotic fly) [2] and the stable hovering of a jellyfish-like flying machine [3] have recently been achieved. Such a technological application is also a motivation for studying flapping flight.

Since there is no muscular system in the frames of the insect wings unlike birds [4], the insect wings are passively deformed by the inertial, elastic, and aerodynamic forces. This deformation of the wings is likely to significantly affect not only the flow around the wings but also the aerodynamic force and torque acting on the wings. In order to reveal the effect of the deformation or flexibility of the wings on the flapping flight of insects, much effort has recently been made with experimental and computational approaches. Zhao *et al.* [5] experimentally measured the aerodynamic forces on flapping wings with variable flexural stiffness. It was found that both the drag and lift forces decreased in magnitude with increasing wing flexibility. At angles of attack greater than 50°, however, the flexible wings generated more lift force than rigid wings. Zheng *et al.* [6] used computational models derived from experiments on free-flying butterflies to evaluate the effects of time-varying camber and twist deformations on the aerodynamic performance. It was found that the observed butterfly wing including both camber and twist deformations improved the aerodynamic performance compared with the rigid wing. In addition, the twist deformation occupied most of the improvement.

In the computational approach to investigate the effect of wing flexibility on the flapping flight, it is worthwhile to consider the wings as flexible membranes and to reproduce the *full* flexibility of the flapping wings [7]. Also, it is meaningful to construct *simple* flexible wings which are composed of some rigid parts connected by torsion springs and to consider

---

[*] kosuzuki@shinshu-u.ac.jp

[†] Present address: Toyota Boshoku Corporation, Aichi 448-8651, Japan.

[‡] masato@shinshu-u.ac.jp; also at Institute of Carbon Science and Technology, Interdisciplinary Cluster for Cutting Edge Research, Shinshu University.

the chordwise and spanwise flexibilities separately. Several studies using such simpler models have focused on the chordwise wing flexibility, since it was reported that the spanwise flexural stiffness is one to two orders of magnitude larger than chordwise flexural stiffness for many insects [8]. Eldredge *et al.* [9] constructed a two-dimensional flexible wing composed of two rigid elliptical cylinders connecting by a torsion spring. The leading portion of the wing was prescribed with hovering kinematics. In this wing, the wing flexibility can be controlled by the spring stiffness of the torsion spring. Cheng and Lan [10] constructed a three-dimensional flexible wing with hovering kinematics in the same way as Eldredge *et al.* [9]. It was found that the chordwise wing flexibility reduced the lift force and the power, and consequently a wing with small flexibility generally achieved a marginally higher efficiency (power-loading coefficient) than the rigid wing. Medina and Eldredge [11] also constructed a three-dimensional wing composed of three rigid plates, i.e., leading, root, and tip portions, and the root and tip portions were deflected actively. Although in this wing the flexibility cannot be controlled, it was found that the root or tip deflection can increase the efficiency in hovering kinematics.

The above-mentioned studies have shown that the chordwise wing flexibility has a significant effect on aerodynamic performance for hovering kinematics. However, the chordwise wing flexibility for other wing kinematics has not been investigated sufficiently. As one of the other wing kinematics, it is worthwhile to consider a butterfly-like flapping wing motion [12], where the wings are flapped downward and backward during downstroke and upstroke to generate the lift and thrust forces, respectively. A similar wing motion has been observed in the forward flight of leaf butterflies (*Kallima inachus*) [13,14], and the vortex structures generated by the butterfly-like flapping wing motion are similar to those generated by actual butterflies, e.g., chestnut tiger butterflies (*Parantica site*) [15], leaf butterflies [14], and tree nymph butterflies (*Idea leuconoe*) [16]. In addition, the butterfly-like flapping wing motion utilizes aerodynamic forces that are parallel to the wing-tip path, i.e., drag-based forces [1,17]. It has been reported that small insects such as fruit flies often use drag-based forces in rapid maneuvers such as sudden starts, stops, and turns [17]. It has been suggested in Ref. [18] that this strategy has been observed in larger insects such as butterflies [19]. Therefore, it is interesting to investigate the chordwise wing flexibility for the butterfly-like flapping wing motion.

A concept model with the butterfly-like flapping wing motion was proposed in the previous study [12]. Hereafter, we will call it the *butterfly model*. In the previous studies, Suzuki and co-workers numerically investigated the effects of wing kinematic parameters [20], wing planform [21], and wing mass [22] on aerodynamic performance in the flapping flight of the butterfly model by using the immersed boundary-lattice Boltzmann method (IB-LBM) [23]. In the present study, in order to advance these researches, we incorporate the chordwise wing flexibility into the butterfly model in the same way as the flexible wing used in Ref. [10] and investigate the effect of chordwise wing flexibility on aerodynamic performance in the flapping flight of the butterfly model. While there are other flight modes in the free flight of insects, e.g., take-off [24,25], climbing flight [26], forward flight [13,14], gliding flight [27], and others, we focus on starting from the resting state and the transitional motion to forward flight. It is noted that we do not focus on the ground effect in the present study (see Sec. IV).

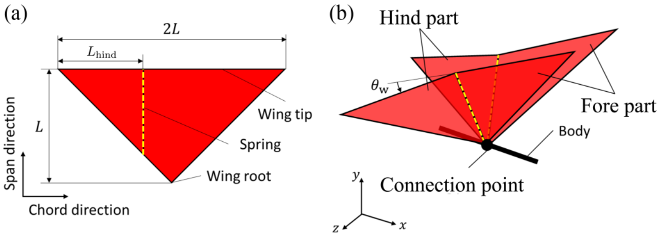

FIG. 1. Illustration of (a) a flexible wing and (b) a butterfly model with two flexible wings and a rod-shaped body.

The paper is organized as follows. In Sec. II we present the butterfly model with chordwise wing flexibility. In Sec. III we explain the governing equations and parameters of the system. The numerical method and the computational parameters are presented in Sec. IV, and results and discussion are shown in Sec. V. We conclude in Sec. VI.

## II. BUTTERFLY MODEL

### A. Components

The butterfly model used in this paper is shown in Fig. 1. The wings of the model are infinitely thin isosceles triangles composed of the fore and hind parts connected by a torsion spring parallel to the span direction as shown in Fig. 1(a). It is noted that the wings effectively have a finite thickness due to the finite resolution of the present simulations and due to the finite support of the volume force in the immersed boundary method (see Sec. IV). Although the fore and hind parts are rigid, the chordwise wing flexibility can be changed by the spring stiffness $K$ of the torsion spring. The motion of the fore part is prescribed as explained in Sec. II B, and the motion of the hind part is determined by calculating the deflection angle $\theta_{\rm w}$ between the fore and hind parts as explained in Sec. III B. The wing length is equal to $L$, and the total wing-tip length is equal to $2L$. The hind wing-tip length is given by $L_{\rm hind}$, and its range is $0 \leqslant L_{\rm hind} \leqslant L$. The wings are flexed in their center lines when $L_{\rm hind} = L$, whereas the wings are completely rigid when $L_{\rm hind} = 0$. The fore and hind parts have the same uniform mass density, and the total mass of the two wings is denoted by $m_{\rm w}$.

The model has a rod-shaped body of length $L_{\rm b} = L$. The wing root is connected to the midpoint of the body. Since the range of the hind wing-tip length $L_{\rm hind}$ is less than or equal to $L$, the fore part is always connected to the body. The mass of the body is denoted by $m_{\rm b}$, and the moment of inertia of the body is given by $I_{\rm b} = m_{\rm b}L_{\rm b}^2/12$. The total mass of the model is given by $M = m_{\rm b} + m_{\rm w}$.

### B. Wing kinematics of the fore part

The butterfly model flaps the wings downward and backward to generate lift and thrust forces, respectively. The motions of the right and left fore parts are prescribed relative to the body and symmetrical with respect to the longitudinal

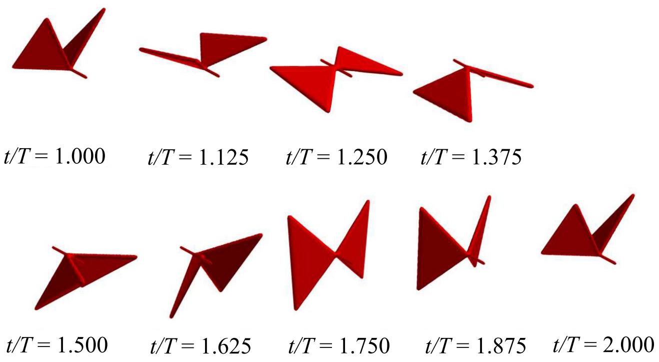

FIG. 2. The wing motion during one period for $t/T \geqslant 1$ when the wings are rigid and $(\theta_\mathrm{m}, \alpha_\mathrm{m}, \gamma) = (45^\circ, 90^\circ, \pi/2)$.

plane. The wing kinematics are a combination of a flapping motion and an attacking motion, described by the flapping angle $\theta$ and the geometric angle of attack (AOA) $\alpha$, respectively. The rotational axis for the geometric AOA is perpendicular to the wing root, and that for the flapping angle is parallel to the wing root. The flapping angle $\theta(t)$ and the geometric AOA $\alpha(t)$ at time $t$ are given as follows:

$$\theta(t) = \theta_\mathrm{m} \cos\left(\frac{2\pi}{T}t\right), \tag{1}$$

$$\alpha(t) = \begin{cases} 0, & \left(0 \leqslant t < \frac{T}{4}\right), \\ \frac{\alpha_\mathrm{m}}{2}\left[1 + \cos\left(\frac{2\pi}{T}t + \gamma\right)\right], & \left(t \geqslant \frac{T}{4}\right), \end{cases} \tag{2}$$

where $\theta_\mathrm{m}$ is the flapping amplitude corresponding to half the stroke amplitude, $\alpha_\mathrm{m}$ is the maximum geometric angle of attack, $T$ is the period of flapping motion, and $\gamma$ is the phase shift.

In our previous study [20], we calculated aerodynamic performance for various sets of the kinematic parameters $(\theta_\mathrm{m}, \alpha_\mathrm{m}, \gamma)$, and we found that the efficiency (the power-loading coefficient) is nearly maximized when $(\theta_\mathrm{m}, \alpha_\mathrm{m}, \gamma) = (45^\circ, 90^\circ, \pi/2)$. In this study, we use this set of the parameters supposing that the butterfly model flies with almost the highest efficiency. Figure 2 shows the wing kinematics when the wings are rigid (i.e., $L_\mathrm{hind} = 0$) and the above set of the parameters is used.

It should be noted that the geometric AOA $\alpha(t)$ given by Eq. (2) is different from that used in Ref. [12] only in the first quarter period of the first wingbeat. If the time derivative of $\alpha(t)$ is not zero at the initial time $t = 0$, the wings have momentum initially due to the wing mass. Therefore, this modification is for avoiding the impulsive start. For more details about the wing kinematics of the model and their formulation in terms of the rotations of the coordinate system, see Ref. [12].

When the deflection angle $\theta_\mathrm{w}$ between the fore and hind parts is given by calculating the equation of motion (see Sec. III B), the motion of the hind part is described by the rotation of the coordinate system fixed to the hind part relative to the fore part. Let the coordinate system fixed to the right fore part be $\Sigma_\mathrm{fore}$, and its origin be located at the wing root. The axes of $\Sigma_\mathrm{fore}$ are denoted by $\xi$, $\eta$, and $\zeta$, where the $\xi$ axis is parallel to the chord direction and the $\eta$ axis is parallel to the span direction. Let the coordinate system fixed to the right hind part be $\Sigma_\mathrm{hind}$, and its axes are denoted by $\xi_\mathrm{hind}$, $\eta_\mathrm{hind}$, and $\zeta_\mathrm{hind}$. Since the torsion spring is parallel to the span direction, $\Sigma_\mathrm{hind}$ is obtained by rotating $\Sigma_\mathrm{fore}$ around the $\eta$ axis by the angle $\theta_\mathrm{w}$. Let $\boldsymbol{e}_\xi$, $\boldsymbol{e}_\eta$, and $\boldsymbol{e}_\zeta$ be three unit vectors along the $\xi$, $\eta$, and $\zeta$ axes, respectively, and $\boldsymbol{e}_{\xi\mathrm{hind}}$, $\boldsymbol{e}_{\eta\mathrm{hind}}$, and $\boldsymbol{e}_{\zeta\mathrm{hind}}$ be three unit vectors along the $\xi_\mathrm{hind}$, $\eta_\mathrm{hind}$, and $\zeta_\mathrm{hind}$ axes, respectively. The vector array $[\boldsymbol{e}_{\xi\mathrm{hind}}, \boldsymbol{e}_{\eta\mathrm{hind}}, \boldsymbol{e}_{\zeta\mathrm{hind}}]$ is given by an orthogonal transformation of $[\boldsymbol{e}_\xi, \boldsymbol{e}_\eta, \boldsymbol{e}_\zeta]$ as

$$[\boldsymbol{e}_{\xi\mathrm{hind}}, \boldsymbol{e}_{\eta\mathrm{hind}}, \boldsymbol{e}_{\zeta\mathrm{hind}}] = [\boldsymbol{e}_\xi, \boldsymbol{e}_\eta, \boldsymbol{e}_\zeta]\boldsymbol{\mathcal{S}}_2(\theta_\mathrm{w}), \tag{3}$$

where $\boldsymbol{\mathcal{S}}_2$ is the orthogonal matrix given by

$$\boldsymbol{\mathcal{S}}_2(\theta_\mathrm{w}) = \begin{bmatrix} \cos\theta_\mathrm{w} & 0 & \sin\theta_\mathrm{w} \\ 0 & 1 & 0 \\ -\sin\theta_\mathrm{w} & 0 & \cos\theta_\mathrm{w} \end{bmatrix}. \tag{4}$$

We assume that the motion of the left hind part is symmetrical to the right hind part with respect to the longitudinal plane. Under this assumption, we use a symmetry boundary condition and simulate only half the butterfly model (see Sec. IV).

## III. GOVERNING EQUATIONS AND NONDIMENSIONAL PARAMETERS

### A. Fluid motion

The fluid motion around the butterfly model is governed by the continuity equation and the Navier-Stokes equation for an incompressible fluid:

$$\nabla \cdot \boldsymbol{u} = 0, \tag{5}$$

$$\frac{\partial \boldsymbol{u}}{\partial t} + (\boldsymbol{u} \cdot \nabla)\boldsymbol{u} = -\frac{1}{\rho_\mathrm{f}}\nabla p + \nu\nabla^2\boldsymbol{u}, \tag{6}$$

where $\boldsymbol{u}$ is the fluid velocity, $p$ is the pressure, $\rho_\mathrm{f}$ is the fluid density, and $\nu$ is the kinematic viscosity of the fluid. We consider the fluid to be air at room temperature (20 °C), and we set $\rho_\mathrm{f} = 1.205\,\mathrm{kg/m^3}$ and $\nu = 1.512 \times 10^{-5}\,\mathrm{m^2/s}$. It should be noted that the gravitational term does not appear in Eq. (6). This is because the pressure $p$ includes the gravitational potential [28]. The no-slip condition must be satisfied on the surface of the model, i.e., the fluid velocity must be equal to the velocity of the wings and the body. It should be noted that the body has a negligible effect on the flow field and the aerodynamic forces for the present model, although the no-slip condition is enforced on the body.

In this study, we take the mean wing-tip speed defined by $U_\mathrm{tip} = 4\theta_\mathrm{m}L/T$ as the characteristic flow speed and the wing length $L$ as the characteristic length. The governing parameter of the above equations is the Reynolds number Re given by

$$\mathrm{Re} = \frac{U_\mathrm{tip}L}{\nu}. \tag{7}$$

It should be noted that the definition of the Reynolds number is the same as that used in Ref. [12].

### B. Wing-body motion

The system of the present model is a six-body problem composed of four rigid flat plates (fore and hind parts in left and right wings) and one rigid rod (body). In order to connect the fore parts and the body and to enforce the flapping angle $\theta(t)$ and the geometric AOA $\alpha(t)$ of the wings relative to the body, we have to consider the appropriate force of constraint and torque of constraint between the wings and the body. In addition, we have to consider the appropriate force of constraint and torque of constraint between the fore and hind parts as well as the torque by the torsion spring. If the Lagrangian formulation is used, however, there is no need to formulate them explicitly.

We define the coordinate system of the flight space with axes $x$, $y$, and $z$, where the positive directions of the $x$ and $y$ axes are the forward and upward directions, respectively. The gravitational acceleration is given by $\boldsymbol{G} = (0, -G, 0)^{\mathrm{T}}$ (where the superscript T represents the transpose of a vector or a matrix), and we set $G = 9.807\,\mathrm{m/s^2}$. Here we assume that the body moves only in the $x$ and $y$ directions and rotates only in the $x$-$y$ plane (pitching motion) for simplicity. Let the position of the center of the body be $\boldsymbol{X}_{\mathrm{b}} = (x_{\mathrm{b}}, y_{\mathrm{b}}, 0)^{\mathrm{T}}$, and the pitching angle be $\theta_{\mathrm{p}}$. In addition, let the deflection angle between the fore and hind parts be $\theta_{\mathrm{w}}$. The motion of the wing-body system is described by the four independent variables $x_{\mathrm{b}}$, $y_{\mathrm{b}}$, $\theta_{\mathrm{p}}$, and $\theta_{\mathrm{w}}$. Let the Lagrangians for the body, the right fore part, and the right hind part be $\mathcal{L}_{\mathrm{body}}$, $\mathcal{L}_{\mathrm{fore}}$, and $\mathcal{L}_{\mathrm{hind}}$, respectively. The Lagrangian for the whole system is given by

$$\mathcal{L} = \mathcal{L}_{\mathrm{body}} + 2\mathcal{L}_{\mathrm{fore}} + 2\mathcal{L}_{\mathrm{hind}}. \tag{8}$$

It should be noted that the Lagrangians for the left fore and hind parts are the same as those for the right fore and hind parts, since it is assumed that the motions of the left parts are symmetrical to the right parts with respect to the longitudinal plane. The detailed forms of these Lagrangians are shown in Appendix A.

The Lagrange equations for the wing-body motion can be obtained as follows:

$$\frac{d}{dt}\left(\frac{\partial \mathcal{L}}{\partial \dot{x}_{\mathrm{b}}}\right) - \frac{\partial \mathcal{L}}{\partial x_{\mathrm{b}}} = F_x^{\mathrm{aero}}, \tag{9}$$

$$\frac{d}{dt}\left(\frac{\partial \mathcal{L}}{\partial \dot{y}_{\mathrm{b}}}\right) - \frac{\partial \mathcal{L}}{\partial y_{\mathrm{b}}} = F_y^{\mathrm{aero}}, \tag{10}$$

$$\frac{d}{dt}\left(\frac{\partial \mathcal{L}}{\partial \dot{\theta}_{\mathrm{p}}}\right) - \frac{\partial \mathcal{L}}{\partial \theta_{\mathrm{p}}} = T^{\mathrm{aero}}, \tag{11}$$

$$\frac{d}{dt}\left(\frac{\partial \mathcal{L}_{\mathrm{hind}}}{\partial \dot{\theta}_{\mathrm{w}}}\right) - \frac{\partial \mathcal{L}_{\mathrm{hind}}}{\partial \theta_{\mathrm{w}}} = T_{\mathrm{hind}}^{\mathrm{aero}}, \tag{12}$$

where $F_x^{\mathrm{aero}}$ and $F_y^{\mathrm{aero}}$ are the $x$ and $y$ components of the aerodynamic force $\boldsymbol{F}^{\mathrm{aero}}$, respectively, $T^{\mathrm{aero}}$ is the total aerodynamic pitching moment around the center of the body, $T_{\mathrm{hind}}^{\mathrm{aero}}$ is the aerodynamic pitching moment acting on the right hind part around the torsion spring, and the dot notation denotes the time derivative.

By substituting Eq. (8) in Eqs. (9)–(12), these equations can be expressed in matrix form for the vector $(\ddot{x}_{\mathrm{b}}, \ddot{y}_{\mathrm{b}}, \ddot{\theta}_{\mathrm{p}}, \ddot{\theta}_{\mathrm{w}})$ as

$$\boldsymbol{\mathcal{M}}\begin{bmatrix}\ddot{x}_{\mathrm{b}}\\ \ddot{y}_{\mathrm{b}}\\ \ddot{\theta}_{\mathrm{p}}\\ \ddot{\theta}_{\mathrm{w}}\end{bmatrix} = \begin{bmatrix}F_x^{\mathrm{aero}} + F_x^{\mathrm{in}}\\ F_y^{\mathrm{aero}} + F_y^{\mathrm{in}} - MG\\ T^{\mathrm{aero}} + T^{\mathrm{in}} + T^{\mathrm{G}}\\ T_{\mathrm{hind}}^{\mathrm{aero}} - K\theta_{\mathrm{w}} + T_{\mathrm{hind}}^{\mathrm{in}} + T_{\mathrm{hind}}^{\mathrm{G}}\end{bmatrix}, \tag{13}$$

where $\boldsymbol{\mathcal{M}}$ is the mass matrix of the system, $F_x^{\mathrm{in}}$ and $F_y^{\mathrm{in}}$ are the $x$ and $y$ components of the inertial force $\boldsymbol{F}^{\mathrm{in}}$, respectively, $T^{\mathrm{in}}$ is the inertial pitching moment, and $T^{\mathrm{G}}$ is the pitching moment due to gravity. The subscript "hind" is put in the variables for the right hind part.

The governing parameters of Eq. (13) are the nondimensional total mass $N_{\mathrm{M}}$, the Froude number Fr, the wing-mass ratio WR, the nondimensional hind wing-tip length $\chi$, and the nondimensional spring stiffness $N_{\mathrm{K}}$ defined as

$$N_{\mathrm{M}} = \frac{M}{\rho_{\mathrm{f}} L^3}, \tag{14}$$

$$\mathrm{Fr} = \frac{U_{\mathrm{tip}}}{\sqrt{LG}}, \tag{15}$$

$$\mathrm{WR} = \frac{m_{\mathrm{w}}}{M}, \tag{16}$$

$$\chi = \frac{L_{\mathrm{hind}}}{L}, \tag{17}$$

$$N_{\mathrm{K}} = \frac{K}{\rho_{\mathrm{f}} L^3 U_{\mathrm{tip}}^2}. \tag{18}$$

The total governing parameters of the whole system are Re, $N_{\mathrm{M}}$, Fr, WR, $\chi$, and $N_{\mathrm{K}}$. In order to calculate free flights of the model in a fluid, we have to determine these six parameters. However, these six parameters are not independent. Actually, the relationship between Re and Fr is given by

$$\frac{\mathrm{Fr}}{\mathrm{Re}} = \frac{\nu}{\sqrt{L^3 G}}. \tag{19}$$

Given the values of $\nu$ in the Earth's atmosphere and $G$, the ratio of Fr to Re is determined by setting the wing length $L$. Therefore, the wing length $L$ is equivalent to the ratio of the Froude number to the Reynolds number in this situation.

## IV. NUMERICAL METHOD AND COMPUTATIONAL PARAMETERS

The numerical method used in this study is the same as that in Ref. [12]; we use the IB-LBM approach [23] to solve Eqs. (5) and (6). The wings and the body of the model are represented by an arrangement of boundary Lagrangian points. In order to enforce the no-slip condition on the model, the volume force is applied at lattice points around the boundary Lagrangian points. Due to the finite support of the volume force, the wings and body have a finite thickness. In our previous study [29], the effective thickness of a flat plate was $2.5\Delta x$ ($\Delta x$ is a lattice spacing) in terms of the accuracy of the velocity profile in the laminar boundary layer. In addition, we checked the effect of the effective thickness by the convergence studies for spatial resolution using the present butterfly model [12,21,22]. As a result, we found that the spatial resolution where $L = 60\Delta x$ for $\mathrm{Re} = 500$ was sufficiently large, since the aerodynamic force and torque as well as the motion of the model for this resolution were not so different from those for a finer resolution. This means that for the present spatial resolution the effective thickness does not have a significant effect.

The distance between the boundary Lagrangian points on the wings is about $\Delta x$. This distance is small enough to prevent the fluid penetrating the wings. Also, the gap between the boundary Lagrangian points on the trailing edge of the fore part and those on the leading edge of the hind part is about $\Delta x$, and the fluid does not penetrate the wings through this gap. Therefore, a finite gap is set between the fore and hind parts numerically, but it has no effect physically. In our preliminary study, the gap did not cause any problems, e.g., source or sink of fluid, peaks in pressure localized at the hinge, or unphysical oscillations in the aerodynamic force.

The aerodynamic force $\boldsymbol{F}^{\mathrm{aero}}$ and torque $\boldsymbol{T}^{\mathrm{aero}}$ are calculated as

$$\boldsymbol{F}^{\mathrm{aero}}(t) = -\sum_{\boldsymbol{x}} \boldsymbol{g}(\boldsymbol{x}, t)(\Delta x)^3, \tag{20}$$

$$\boldsymbol{T}^{\mathrm{aero}}(t) = -\sum_{\boldsymbol{x}} (\boldsymbol{x} - \boldsymbol{X}_{\mathrm{b}}) \times \boldsymbol{g}(\boldsymbol{x}, t)(\Delta x)^3, \tag{21}$$

where $\sum_{\boldsymbol{x}}$ describes the summation over all lattice points $\boldsymbol{x}$, and $\boldsymbol{g}(\boldsymbol{x}, t)$ is the volume force which is applied at a lattice point $\boldsymbol{x}$ in order to enforce the no-slip condition on the model in the immersed boundary method. It is noted that $\boldsymbol{T}^{\mathrm{aero}}$ in Eq. (21) is assumed to have only the $z$ component, i.e., the pitching moment $T^{\mathrm{aero}}$. The aerodynamic pitching moment $T^{\mathrm{aero}}_{\mathrm{hind}}$ acting on the right hind part around the torsion spring is given by

$$T^{\mathrm{aero}}_{\mathrm{hind}}(t) = -\sum_{\boldsymbol{X} \in \mathrm{hind}} \boldsymbol{n} \cdot \boldsymbol{g}(\boldsymbol{X}, t)\, l(\boldsymbol{X})\, \Delta V, \tag{22}$$

where $\sum_{\boldsymbol{X} \in \mathrm{hind}}$ describes the summation over the boundary Lagrangian points $\boldsymbol{X}$ in the right hind part, $\boldsymbol{n}$ is the unit vector perpendicular to the right hind part, $\boldsymbol{g}(\boldsymbol{X}, t)$ is the volume force at a boundary Lagrangian point $\boldsymbol{X}$, $l(\boldsymbol{X})$ is the distance between the torsion spring and the boundary Lagrangian point $\boldsymbol{X}$, and $\Delta V$ is the small volume element where the volume force $\boldsymbol{g}(\boldsymbol{X}, t)$ is applied. In this calculation, the internal mass effect [23] is neglected, since the model has effective volume but converges to a thin object with no volume in the limit $\Delta x \to 0$. The position and velocity of the boundary Lagrangian points on the wings and the body are updated by orthogonal transformation of the coordinate systems fixed to the wings and the body relative to that fixed to the flight space. For details of the numerical method, see Ref. [23].

The validation of the numerical method and the convergence studies for temporal and spatial resolutions have been extensively checked in Refs. [12,21,22]. In addition, Engels *et al.* [30] simulated the same problem as Ref. [12] to validate their proposed method (a Fourier method with volume penalization), and they reported that their result for the free flight of the butterfly model had a good agreement with that obtained in Ref. [12]. The validation for a flexible wing is shown in Appendix B.

The computational domain is the same as that used in Ref. [21]: we use a cuboid of $18L \times 12L \times 12L$. The $x$, $y$, and $z$ axes are fixed to the domain, and we denote the directions of the $x$ and $y$ axes as forward and upward, respectively. The boundary condition on two sides perpendicular to the $x$ axis is the periodic boundary condition, and on the other sides the no-slip condition is used. The center of the body is initially located at the center of the domain. The size of the computational domain is so large that the ground effect is not significant, since in the previous study [12] the aerodynamic forces obtained when the domain size was $12L \times 6L \times 6L$ were almost the same as those obtained when the domain size was $12L \times 12L \times 12L$. The domain is initially filled with a stationary fluid at uniform pressure. We use a multiblock grid [31] in order to save computation time. The multiblock grid is composed of a fine grid with a lattice spacing $\Delta x$ and a coarse grid with $2\Delta x$. The size of the inner fine grid is set to $4L \times 4L \times 4L$, in order to confine the butterfly model to the inner fine grid including a sufficient margin. In order to reduce the computational cost, we calculate one-half of the computational domain with the mirror boundary condition on the longitudinal plane which passes through the center of the domain and is perpendicular to $z$ axis. This implies that the flow field is assumed to be symmetrical with respect to the longitudinal plane. We simulate the free flights of the butterfly model for various Reynolds numbers in the range $300 \leqslant \mathrm{Re} \leqslant 1000$, which covers the typical Reynolds numbers of small insects. The spatial and temporal resolutions for each Re are shown in Table I.

TABLE I. Spatial and temporal resolutions for various values of the Reynolds number Re. The wing length $L$ and the flapping period $T$ are multiples of the lattice spacing $\Delta x$ and the time step $\Delta t$, respectively.

| Re | $L$ | $T$ |
|---|---|---|
| 300 | $50\Delta x$ | $6000\Delta t$ |
| 500 | $60\Delta x$ | $6000\Delta t$ |
| 700 | $86\Delta x$ | $8000\Delta t$ |
| 1000 | $120\Delta x$ | $12\,000\Delta t$ |

In the present study, we investigate the effect of chordwise wing flexibility on aerodynamic performance by changing the nondimensional spring stiffness $N_{\mathrm{K}}$ and the nondimensional hind wing-tip length $\chi$. The range of the Reynolds number is shown in Table I. As for the other governing parameters (i.e., the nondimensional total mass $N_{\mathrm{M}}$, the Froude number Fr, and the wing-mass ratio WR), we consider two sets of the parameters for a small butterfly (*Janatella leucodesima*) [32] and a fruit fly [4] as shown in Table II. It should be noted that the ratio of the Froude number to the Reynolds number is determined by the wing length $L$ as mentioned in Sec. III B. In the present study, we consider the parameter set of a fruit fly as well as that of a butterfly in order to investigate the effect of the length scale $L$. In addition, in the development of MAVs, the small length scale is likely to be attractive. Therefore, we consider the parameter set of a fruit fly as a typical set for a small length scale. It should be noted that the actual Reynolds

TABLE II. The wing length $L$, the nondimensional total mass $N_{\mathrm{M}}$, the wing-mass ratio WR, and the ratio of the Froude number Fr to the Reynolds number Re for a small butterfly (*Janatella leucodesima*) and a fruit fly.

| | $L$ (mm) | $N_{\mathrm{M}}$ | WR | Fr/Re |
|---|---|---|---|---|
| Set 1 (*J. leucodesma*) | 18.1 | 3.36 | 0.1 | $1.98 \times 10^{-3}$ |
| Set 2 (fruit fly) | 3.0 | 61 | 0.0048 | 0.029 |

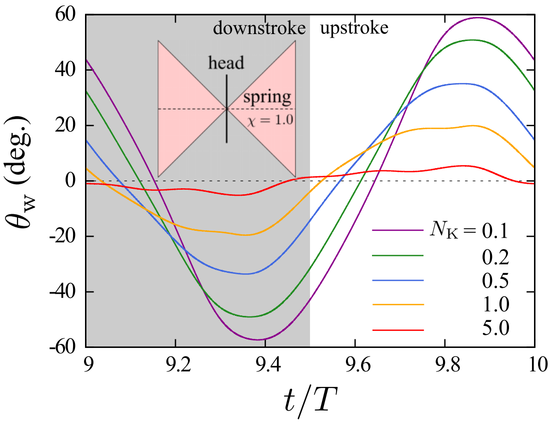

FIG. 3. Time variations of the deflection angle $\theta_w$ for various values of the nondimensional spring stiffness $N_K$ when the body of the model is fixed, $\chi = 1.0$, Re = 500, and the other governing parameters are given as Set 1 in Table II.

number for a *Janatella leucodesma* is Re = 1190 and that for a fruit fly is Re = 620 in the present definition of the Reynolds number using the wing length $L$ as the characteristic length (if the Reynolds number is defined by using the mean wing chord length, Re $\simeq$ 100 for a fruit fly [4]). Table II does not include the values of Re so that we separately treat Re and the parameter set shown in this table.

## V. RESULTS AND DISCUSSION

In this section, we investigate the effect of chordwise wing flexibility on aerodynamic performance in flapping flight of the butterfly model. First, we calculate aerodynamic performance for various values of the nondimensional spring stiffness $N_K$ and nondimensional hind wing-tip length $\chi$ when the body of the model is fixed. In addition, we investigate how the effect of chordwise wing flexibility is changed when the Reynolds number Re and the other governing parameters are changed. Then we investigate the effects of chordwise wing flexibility on the translational motion and on the rotational motion of the butterfly model through free-flight simulations with and without pitching rotation.

### A. Aerodynamic performance when the body of the model is fixed

#### *1. Effects of the nondimensional spring stiffness $N_K$ and the nondimensional hind wing-tip length $\chi$*

First, we calculate the deflection angle $\theta_w$ for various values of the nondimensional spring stiffness $N_K$ when the body of the model is fixed, $\chi = 1.0$, Re = 500, and the other governing parameters are given as Set 1 in Table II. In this simulation, we neglect Eqs. (9)–(11) and consider Eq. (12) alone. Figure 3 shows the time variations of the deflection angle $\theta_w$ for various values of $N_K$ for $9.0 \leqslant t/T \leqslant 10$. It should be noted that the simulations are conducted until $t/T = 20$, but the results during each stroke are almost the same after $t/T = 9$. Thus, we present the results of the 10th period here. We can see from this figure that the amplitude of $\theta_w$ significantly increases as $N_K$ decreases, and the wings are so flexible that $\theta_w$ can reach 60° when $N_K = 0.1$, whereas the wings are nearly rigid when $N_K = 5.0$. In addition, the phase of the curves of $\theta_w$ delays as $N_K$ decreases. This result suggests that aerodynamic performance will be significantly affected by the deformation of the wings in the range $0.1 \leqslant N_K \leqslant 5.0$.

Then we calculate aerodynamic performance for various values of the nondimensional spring stiffness $N_K$ for the same condition as above. We calculate the following aerodynamic performance factors, i.e., the lift coefficient $C_L$, the thrust coefficient $C_T$, the pitching moment coefficient $C_M$, and the power coefficient $C_P$:

$$C_L = \frac{F_y^{\text{aero}}}{0.5\rho_f U_{\text{tip}}^2 (2S)}, \tag{23}$$

$$C_T = \frac{F_x^{\text{aero}}}{0.5\rho_f U_{\text{tip}}^2 (2S)}, \tag{24}$$

$$C_M = \frac{T^{\text{aero}}}{0.5\rho_f U_{\text{tip}}^2 (2S)L}, \tag{25}$$

$$C_P = \frac{\int_{\text{wing}} (\boldsymbol{\sigma} \cdot \boldsymbol{n}) \cdot \boldsymbol{u}_{\text{local}}\, dS}{0.5\rho_f U_{\text{tip}}^3 (2S)}, \tag{26}$$

where $S$ is the area of one wing (i.e., equal to $L^2$), $\boldsymbol{\sigma}$ is the stress tensor on the wing surface, $\boldsymbol{n}$ is the unit normal vector on the wing surface pointing to the fluid (i.e., $\boldsymbol{\sigma} \cdot \boldsymbol{n}$ is the local stress acting on the fluid by a unit area of the wing surface), and $\boldsymbol{u}_{\text{local}}$ is the flow velocity at the point. Also, $\int_{\text{wing}} dS$ means the integral over the wings. Therefore, the power coefficient $C_P$ represents the nondimensional form of the power expenditure to move the wings against the aerodynamic force. It should be noted that in the calculation of $C_P$ we do not calculate the stress tensor $\boldsymbol{\sigma}$ directly but use the volume force $\boldsymbol{g}(\boldsymbol{X}, t)$, which is applied on the boundary Lagrangian points $\boldsymbol{X}$ in order to enforce the no-slip condition on these points (see Ref. [20]).

Figure 4 shows the time variations of $C_L$, $C_T$, $C_M$, and $C_P$ for various values of $N_K$ for $9.0 \leqslant t/T \leqslant 10$. As seen in Fig. 4(a), the positive lift is produced during downstroke and the negative lift force is produced during upstroke even when the wings are highly flexible. This is attributed to the wing kinematics that the wings are flapped downward and backward during downstroke and upstroke, respectively. A similar phenomenon can be seen from other numerical results using more realistic butterfly models whose wing kinematics were derived directly from those of actual butterflies [13,15]. On the other hand, in Fig. 4(b), the positive thrust is produced during upstroke and the negative thrust force is produced during downstroke. This is because the roles of the downstroke and the upstroke in the lift coefficient are equivalent to the upstroke and the downstroke in the thrust coefficient, respectively.

We can see from Figs. 4(a) and 4(b) that the positive peak of $C_L$ during the downstroke and that of $C_T$ during the upstroke significantly decrease as $N_K$ decreases, i.e., wing flexibility increases. This is because the effective area of the wings decreases due to their deformation. This shows lift and thrust deteriorations due to the chordwise wing flexibility. In addition, we can see that the small peak of $C_L$ around $t/T = 9.75$ (i.e., when the fore part is almost horizontal) and that

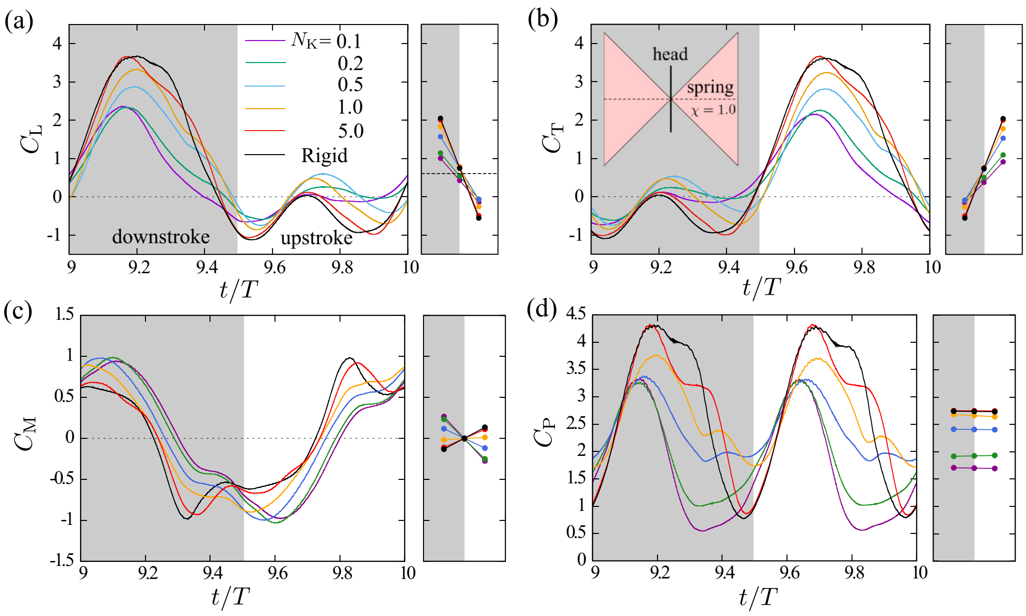

FIG. 4. Time variations of (a) lift coefficient $C_L$, (b) thrust coefficient $C_T$, (c) pitching moment coefficient $C_M$, and (d) power coefficient $C_P$ for various values of the nondimensional spring stiffness $N_K$ when the body of the model is fixed, $\chi = 1.0$, Re $= 500$, and the other governing parameters are given as Set 1 in Table II. Each figure has a small subfigure in the right-hand side. In these subfigures, the left, right, and central bullets indicate the time-averaged values in the downstroke, upstroke, and full cycle, respectively. In the subfigure of panel (a), the dotted line indicates the nondimensional weight force of a *Janatella leucodesima* equal to 0.605.

of $C_T$ around $t/T = 9.25$ (i.e., when the fore part is almost vertical) increase as $N_K$ decreases in the range $0.5 \leqslant N_K$. This shows lift and thrust enhancements due to the chordwise wing flexibility. This is attributed to the fact that the flexible wings can generate not only the lift (thrust) force but also the thrust (lift) force due to their deformation even when the wings are horizontal (vertical). We will discuss the mechanism of the lift and thrust enhancements later by observing the vortex and pressure fields. We can see from Fig. 4(c) that the phase of the peaks of $C_M$ delays as $N_K$ decreases, although the values of the peaks are not so dependent on $N_K$. This is because the motions of the hind parts delay relative to those of the fore parts due to the deformation of the wings, although the distance between the trailing edge of the hind part and the wing root does not change for $\chi = 1.0$. We can see from Fig. 4(d) that the magnitude of $C_P$ significantly decreases as $N_K$ decreases, which is consistent with the decrease in the aerodynamic forces shown in Figs. 4(a) and 4(b).

In order to discuss the mechanism of the lift and thrust enhancements due to the chordwise wing flexibility, we observe the vortex and pressure fields around the flexible wings. Figure 5 shows the vortex structure visualized by the $Q$ criterion around the butterfly model, and the color map of the pressure for various cross sections of the right wing at $t/T = 9.23$, i.e., when the fore part is almost horizontal. The $Q$ criterion is the second invariant of the velocity gradient tensor [33] given by

$$Q = -\frac{\partial u_i}{\partial x_j}\frac{\partial u_j}{\partial x_i}, \tag{27}$$

where $i, j = x, y, z$ represent the Cartesian coordinates and the summation convention is used. The $Q$ criterion identifies low-pressure vortex structures. We can see from Figs. 5(a-1) and 5(a-2) that the wing-tip vortex (WTV) and the leading-edge vortex (LEV) appear on the upper surface of the wings, and they are connected at the corner of the wings. Like an actual butterfly, the WTV and the LEV are considered to be a major cause of the lift and thrust generation of the present model.

We can see from Fig. 5(b) that the low-pressure regions appear in the upper side of the wing, whereas the high-pressure regions appear in the lower side. Due to this pressure distribution, the lift force has a large positive value at this time. This pressure distribution can be caused by the vortices (WTV and LEV) on the upper surface of the wing and by the increase in the pressure of the air in the lower side. From Figs. 5(b-1), 5(b-2), and 5(b-3), it can be seen that the low-pressure region is attached near the leading edge on the upper surface of the wing and gradually comes off as it gets closer to the wing tip. It is likely to be induced by the LEV. From Figs. 5(b-4) and 5(b-5), it can be seen that the low-pressure region appears near the wing tip on the upper surface of the wing. It is likely to be induced by the WTV. On the other hand, the high-pressure region appears on the lower side of the wing for all cross sections, because the downward speed of the wings is maximum around this time, and it is likely to be larger than the downward speed of the ambient air. Therefore, the air in the lower side is pressed by the wings, and consequently the pressure increases in this region.

From this pressure distribution, we can explain the mechanism of the thrust enhancement due to the chordwise wing flexibility around $t/T = 9.25$. We can see from Fig. 5(b) that the low- and high-pressure regions cover not only the fore part but also the hind part. This pressure difference between the upper and lower surfaces of the hind part must cause the aerodynamic force perpendicular to the hind

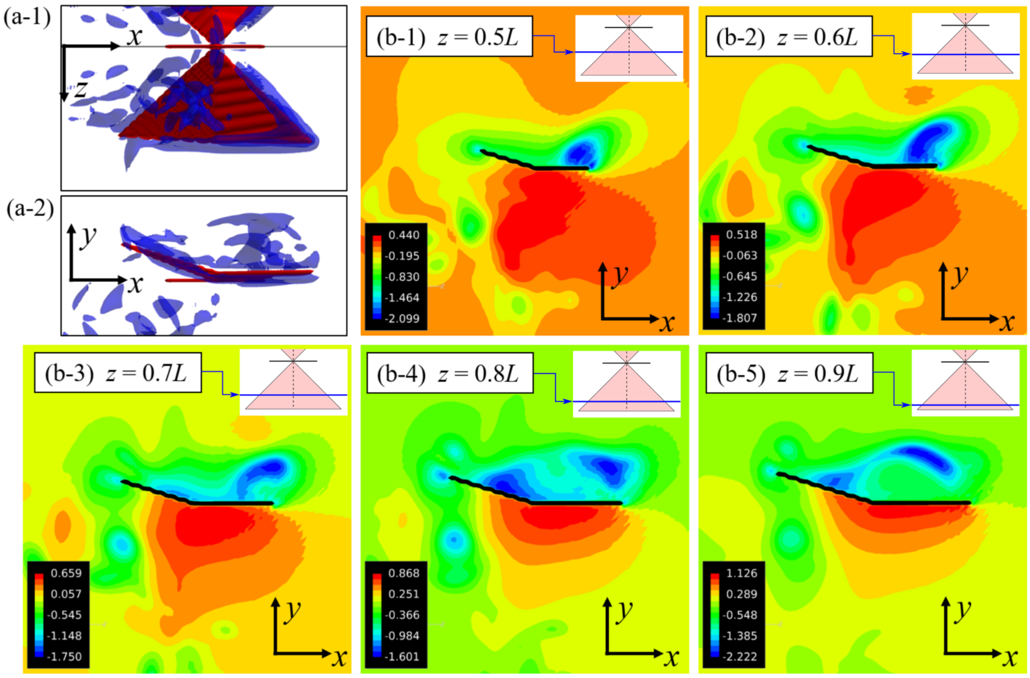

FIG. 5. Vortex structures viewed from (a-1) the upper side and (a-2) the right side of the butterfly model, and (b) the color maps of the pressure fields on the plane perpendicular to the $z$ axis for various positions relative to the wing root at $t/T = 9.23$ when the body of the model is fixed, $N_{\mathrm{K}} = 1.0$, $\chi = 1.0$, Re $= 500$, and the other governing parameters are given as Set 1 in Table II. In (a-1) and (a-2), the model is shown in red, and the isosurface of the $Q$ criterion $[Q = 50(U_{\mathrm{ref}}/L_{\mathrm{ref}})^2]$ is shown in blue. In (b-1)–(b-5), the wing chord is shown in black, and the color map shows the nondimensional pressure, i.e., $(p - p_0)/(\rho_{\mathrm{f}} U_{\mathrm{tip}}^2)$, where $p_0$ is the initial value of the pressure.

part. Since the hind part is inclined by about 20° from the horizontal plane, the aerodynamic force has not only the vertical component but also the horizontal component. The vertical component contributes the lift force, whereas the horizontal component contributes the thrust force. Therefore, the flexible wings can generate not only the lift force but also the thrust force due to their deformation even when the wings are horizontal. Also, the lift enhancement due to the chordwise wing flexibility around $t/T = 9.75$ can be explained in the same way.

The time-averaged values of $C_{\mathrm{L}}$, $C_{\mathrm{T}}$, and $C_{\mathrm{P}}$ are important indices of the aerodynamic performance. Let the time-averaged values of $C_{\mathrm{L}}$, $C_{\mathrm{T}}$, and $C_{\mathrm{P}}$ in one stroke be $\overline{C_{\mathrm{L}}}$, $\overline{C_{\mathrm{T}}}$, and $\overline{C_{\mathrm{P}}}$, respectively. We define the power-loading coefficient as

$$C_{\mathrm{PL}} = \frac{\sqrt{\overline{C_{\mathrm{L}}}^2 + \overline{C_{\mathrm{T}}}^2}}{\overline{C_{\mathrm{P}}}}. \tag{28}$$

It should be noted that in this study the power-loading coefficient is defined by using the magnitude of the vector $(\overline{C_{\mathrm{T}}}, \overline{C_{\mathrm{L}}})$, while in general it is defined by the ratio of the lift coefficient to the power coefficient. Since the present butterfly model generates the thrust force as well as the lift force, the above definition should be more appropriate as an index of efficiency.

Figure 6 shows $\overline{C_{\mathrm{L}}}$, $\overline{C_{\mathrm{T}}}$, $\overline{C_{\mathrm{P}}}$, and $C_{\mathrm{PL}}$ relative to the values for the rigid wings at Re $= 500$ (see Table III) as the functions of $N_{\mathrm{K}}$. In addition, this figure contains the results for various values of the nondimensional hind wing-tip length $\chi$. It should be noted that the time-averaged value of $C_{\mathrm{M}}$ is not shown in this table, since it is more than two orders of magnitude smaller than the peak value, i.e., negligibly small. We can see from Figs. 6(a) and 6(b) that in the result when $\chi = 1.0$,

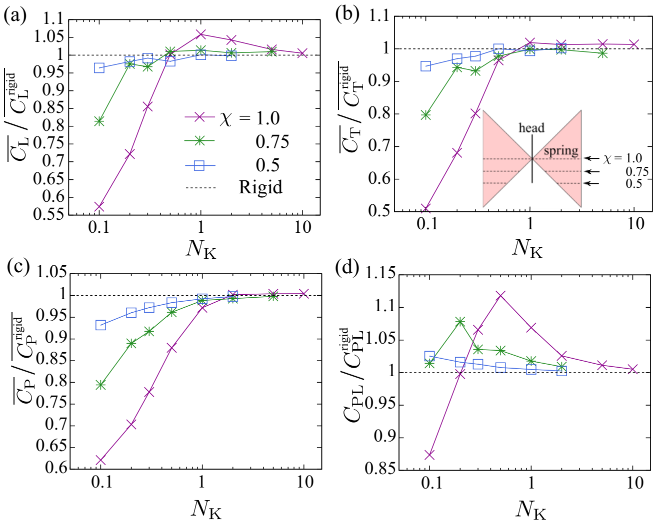

FIG. 6. The ratios of (a) time-averaged lift coefficient $\overline{C_{\mathrm{L}}}$, (b) time-averaged thrust coefficient $\overline{C_{\mathrm{T}}}$, (c) time-averaged power coefficient $\overline{C_{\mathrm{P}}}$, and (d) power-loading coefficient $C_{\mathrm{PL}}$ to the values for the rigid wings $\overline{C_{\mathrm{L}}^{\mathrm{rigid}}}$, $\overline{C_{\mathrm{T}}^{\mathrm{rigid}}}$, $\overline{C_{\mathrm{P}}^{\mathrm{rigid}}}$, and $C_{\mathrm{PL}}^{\mathrm{rigid}}$, respectively, as the functions of the nondimensional spring stiffness $N_{\mathrm{K}}$ for various values of the nondimensional hind wing-tip length $\chi$ when the body of the model is fixed, Re $= 500$, and the other governing parameters are given as Set 1 in Table II.

TABLE III. The time-averaged lift coefficient $\overline{C_\mathrm{L}^\mathrm{rigid}}$, the time-averaged thrust coefficient $\overline{C_\mathrm{T}^\mathrm{rigid}}$, the time-averaged power coefficient $\overline{C_\mathrm{P}^\mathrm{rigid}}$, and the power-loading coefficient $C_\mathrm{PL}^\mathrm{rigid}$ obtained by the rigid wings for various values of the Reynolds number Re.

| Re | $\overline{C_\mathrm{L}^\mathrm{rigid}}$ | $\overline{C_\mathrm{T}^\mathrm{rigid}}$ | $\overline{C_\mathrm{P}^\mathrm{rigid}}$ | $C_\mathrm{PL}^\mathrm{rigid}$ |
|---|---|---|---|---|
| 300 | 0.718 | 0.688 | 2.91 | 0.341 |
| 500 | 0.744 | 0.744 | 2.74 | 0.401 |
| 700 | 0.773 | 0.767 | 2.60 | 0.419 |
| 1000 | 0.802 | 0.789 | 2.49 | 0.452 |

$\overline{C_\mathrm{L}}$ and $\overline{C_\mathrm{T}}$ have their maximum values around $N_\mathrm{K} = 1.0$, and these values exceed the values for the rigid wings. This means that when we use an appropriate spring stiffness, the lift and thrust can be enhanced in terms of the time-averaged values. The appropriate spring stiffness can be determined by the balance between the lift and thrust enhancements and deteriorations due to the chordwise wing flexibility explained above. In addition, we can see that the curves of $\overline{C_\mathrm{L}}$ and $\overline{C_\mathrm{T}}$ get closer to the result for the rigid wings as $\chi$ decreases, and their maximum values decrease. This means that the effect of chordwise wing flexibility decreases as $\chi$ decreases, because a small value of $\chi$ makes the area of the hind parts small.

We can see from Fig. 6(c) that $\overline{C_\mathrm{P}}$ increases with $N_\mathrm{K}$ for all the values of $\chi$, and tends to the result for the rigid wings. The power expenditure for the flexible wings is determined by the balance between the lift and thrust enhancements and deteriorations due to the chordwise wing flexibility. However, the effect of the lift and thrust enhancements on the power expenditure seems to be smaller than their deteriorations, because the thrust enhancement occurs when the velocity of the wings is almost vertical, i.e., perpendicular to the thrust force, and consequently the thrust enhancement does not affect the power expenditure. For the same reason, the lift enhancement does not affect the power expenditure either. We can see from Fig. 6(d) that the value of $C_\mathrm{PL}$ for the flexible wings is larger than that for the rigid wings except when $N_\mathrm{K}$ is very small. In addition, we can see that $C_\mathrm{PL}$ has its maximum value at an appropriate value of $N_\mathrm{K}$ depending on the value of $\chi$. This suggests that the chordwise wing flexibility can improve the aerodynamic efficiency as well as the lift and thrust forces when the body is fixed.

### *2. Effect of the Reynolds number Re and the other governing parameters*

We investigate how the effect of chordwise wing flexibility shown in Sec. V A 1 is changed when the Reynolds number Re is changed in the range $300 \leqslant \mathrm{Re} \leqslant 1000$. We set $\chi = 1.0$ and use Set 1 shown in Table II as the other governing parameters. Table III shows the aerodynamic performance factors obtained by the rigid wings for various values of Re. By using them as the reference values, we calculate the relative values of $\overline{C_\mathrm{L}}$, $\overline{C_\mathrm{T}}$, $\overline{C_\mathrm{P}}$, and $C_\mathrm{PL}$ for the flexible wings as shown in Fig. 7. We can see from this figure that all the aerodynamic performance factors decrease relative to those values for the rigid wings as Re increases. However, the tendencies of these factors for $N_\mathrm{K}$ are similar to each other. Therefore, the effect of chordwise wing flexibility on aerodynamic performance is not so dependent on the Reynolds number Re when the body of the model is fixed.

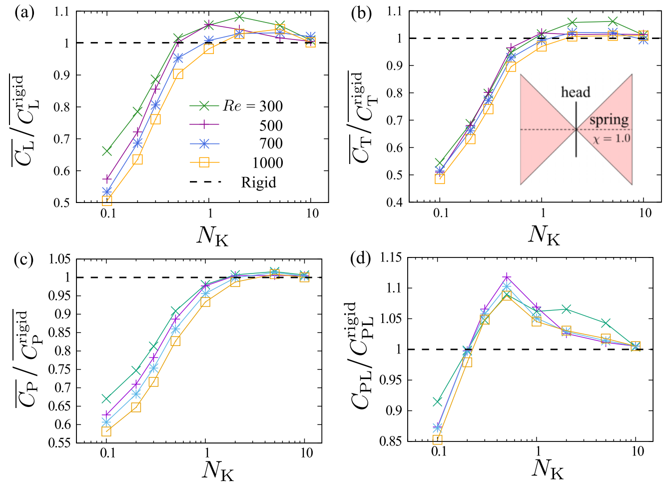

FIG. 7. The ratios of (a) time-averaged lift coefficient $\overline{C_\mathrm{L}}$, (b) time-averaged thrust coefficient $\overline{C_\mathrm{T}}$, (c) time-averaged power coefficient $\overline{C_\mathrm{P}}$, and (d) power-loading coefficient $C_\mathrm{PL}$ to the values for the rigid wings $\overline{C_\mathrm{L}^\mathrm{rigid}}$, $\overline{C_\mathrm{T}^\mathrm{rigid}}$, $\overline{C_\mathrm{P}^\mathrm{rigid}}$, and $C_\mathrm{PL}^\mathrm{rigid}$, respectively, as the functions of the nondimensional spring stiffness $N_\mathrm{K}$ for various values of the Reynolds number Re when the body of the model is fixed, $\chi = 1.0$, and the other governing parameters are given as Set 1 in Table II.

Then we investigate how the effect of chordwise wing flexibility is changed when the other governing parameters are changed. We set $\chi = 1.0$ and $\mathrm{Re} = 500$. Figure 8 shows $\overline{C_\mathrm{L}}$, $\overline{C_\mathrm{T}}$, $\overline{C_\mathrm{P}}$, and $C_\mathrm{PL}$ relative to the values for the rigid wings at $\mathrm{Re} = 500$ (see Table III) as the functions of $N_\mathrm{K}$ for Sets 1

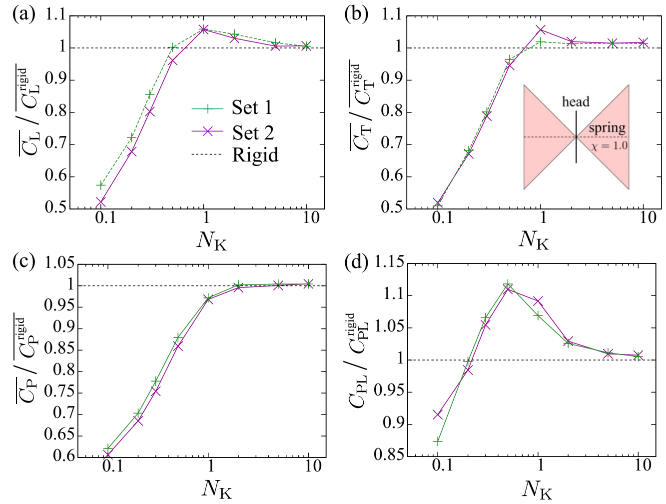

FIG. 8. The ratios of (a) time-averaged lift coefficient $\overline{C_\mathrm{L}}$, (b) time-averaged thrust coefficient $\overline{C_\mathrm{T}}$, (c) time-averaged power coefficient $\overline{C_\mathrm{P}}$, and (d) power-loading coefficient $C_\mathrm{PL}$ to the values for the rigid wings $\overline{C_\mathrm{L}^\mathrm{rigid}}$, $\overline{C_\mathrm{T}^\mathrm{rigid}}$, $\overline{C_\mathrm{P}^\mathrm{rigid}}$, and $C_\mathrm{PL}^\mathrm{rigid}$, respectively, as the functions of the nondimensional spring stiffness $N_\mathrm{K}$ for the two sets of parameters shown in Table II when the body of the model is fixed, $\chi = 1.0$, and $\mathrm{Re} = 500$.

and 2 shown in Table II. We can see from this figure that the tendencies of these aerodynamic performance factors for $N_{\mathrm{K}}$ are almost the same. Therefore, the effect of chordwise wing flexibility on aerodynamic performance is almost independent of the other governing parameters as well.

#### *3. The ratio between the wingbeat and natural frequencies*

The ratio between the wingbeat and natural frequencies have been often used to characterize the flexibility (e.g., Ref. [34]). The wingbeat frequency of the present butterfly model is given as

$$\omega_{\mathrm{f}} = \frac{2\pi}{T}. \tag{29}$$

The natural frequency of the hind part can be defined by using the moment of inertia of the hind part around the torsion spring $I_{\mathrm{w}}^{\mathrm{hind}} = m_{\mathrm{w}}^{\mathrm{hind}} S_{\xi\xi}^{\mathrm{hind}}/2$ (see Appendix A) as

$$\omega_{\mathrm{n}} = \sqrt{\frac{K}{I_{\mathrm{w}}^{\mathrm{hind}}}}. \tag{30}$$

The ratio between the above frequencies can be expressed by using the flapping amplitude $\theta_{\mathrm{m}}$, the wing-mass ratio WR, the nondimensional total mass $N_{\mathrm{M}}$, the nondimensional hind wing-tip length $\chi$, and the nondimensional spring coefficient $N_{\mathrm{K}}$ as

$$\frac{\omega_{\mathrm{f}}}{\omega_{\mathrm{n}}} = \frac{\pi}{4\sqrt{6}\theta_{\mathrm{m}}} \sqrt{\mathrm{WR}\, N_{\mathrm{M}}} \frac{\chi^2}{\sqrt{N_{\mathrm{K}}}}. \tag{31}$$

From Fig. 6(d), the power-loading coefficient $C_{\mathrm{PL}}$ has its maximum value at $N_{\mathrm{K}} \simeq 0.5$ for $\chi = 1.0$ and at $N_{\mathrm{K}} \simeq 0.2$ for $\chi = 0.75$. The corresponding values of $\omega_{\mathrm{f}}/\omega_{\mathrm{n}}$ are 0.335 and 0.298 for $\chi = 1.0$ and 0.75, respectively. These values are comparable with 1/3, which is consistent with the results of a two-dimensional hovering wing with chordwise flexibility [34]. Therefore, the appropriate value of $N_{\mathrm{K}}$ which gives the maximum value of $C_{\mathrm{PL}}$ is given when $\omega_{\mathrm{f}}/\omega_{\mathrm{n}} \simeq 1/3$ even in the present butterfly model.

From Fig. 7(d), the appropriate value of $N_{\mathrm{K}}$ which gives the maximum value of $C_{\mathrm{PL}}$ is not so dependent on the Reynolds number Re. This is consistent with the results of a two-dimensional hovering wing with chordwise flexibility [34]. In addition, this is also consistent with the fact that the wing deformation is mostly determined not by the aerodynamic force but by the wing inertial and elastic forces in a hawk moth [35].

From Fig. 8, the aerodynamic performance factors as the functions of $N_{\mathrm{K}}$ are not so dependent on the other governing parameters. This might be because $\omega_{\mathrm{f}}/\omega_{\mathrm{n}}$ as the function of $N_{\mathrm{K}}$ for Set 1 is comparable with that for Set 2. Actually, we can calculate $\omega_{\mathrm{f}}/\omega_{\mathrm{n}}$ as $0.237 \times \chi^2/\sqrt{N_{\mathrm{K}}}$ for Set 1 and $0.221 \times \chi^2/\sqrt{N_{\mathrm{K}}}$ for Set 2 from Eq. (31). If the aerodynamic performance factors are mostly determined by the value of $\omega_{\mathrm{f}}/\omega_{\mathrm{n}}$, it is a natural consequence that the results for Set 1 are almost the same as those for Set 2.

From the above discussion, we can see that the aerodynamic performance when the body of the present model is fixed is mostly determined by the ratio between the wingbeat and natural frequencies $\omega_{\mathrm{f}}/\omega_{\mathrm{n}}$, and the appropriate value of $N_{\mathrm{K}}$ which gives the maximum value of $C_{\mathrm{PL}}$ is given when $\omega_{\mathrm{f}}/\omega_{\mathrm{n}} \simeq 1/3$.

### B. Free-flight simulations

In this section we simulate the free flight of the butterfly model with chordwise wing flexibility.

#### *1. Without rotation*

First, we simulate the free flight without rotation, i.e., we neglect Eq. (11), and solve Eqs. (9), (10), and (12). We set $\theta_{\mathrm{p}} = \mathrm{const} = 0^\circ$. This means that the body of the model does not rotate in the pitching direction as well as in the yawing and rolling directions. From a physical viewpoint, this means that the inertia moment of the body is assumed to be infinitely large, while the mass of the model is finite. Otherwise, attitude control is assumed to be perfectly achieved and to have no effect on the translational motion of the body. Indeed, both assumptions are unrealistic. However, the aim of this simulation is to investigate the effect of chordwise wing flexibility on the translational motion of the model separately from the rotational motion. In this simulation, we consider the following two cases: (i) when $\chi = 1.0$, $\mathrm{Re} = 1000$, and the other governing parameters are given as Set 1, which is close to the set of parameters for a small butterfly (*J. leucodesma*), and (ii) when $\chi = 1.0$, $\mathrm{Re} = 500$, and the other governing parameters are given as Set 2, which is close to the set of parameters for a fruit fly.

Figure 9 shows the time variations of the deflection angle $\theta_{\mathrm{w}}$ and the trajectories of the center of the body for case (i). It should be noted that Fig. 9(a) shows the results during the fourth period, since the simulation for $N_{\mathrm{K}} = 0.1$ was stopped just after $t = 4T$ due to the collision between the inner fine grid and the bottom wall. We can see from this figure that the curves of $\theta_{\mathrm{w}}$ are similar to the results shown in Fig. 3 which were obtained when the body of the model is fixed, although their amplitudes have small deviation within ±10°. This small deviation is caused by the vertical oscillations of the body motion during one period shown in Fig. 9(b). We can see from Fig. 9(b) that the butterfly model can go forward and upward against gravity except when $N_{\mathrm{K}} = 0.1$, and the trajectory reaches the most upward position when $N_{\mathrm{K}} = 1.0$. This suggests that the model can fly most effectively when $N_{\mathrm{K}} = 1.0$ for case (i). Although the most effective $N_{\mathrm{K}}$ is slightly different from the value suggested in Fig. 7 (around $N_{\mathrm{K}} = 5.0$ when $\mathrm{Re} = 1000$) presumably due to the increase in the forward speed, this result is consistent with the results obtained when the body is fixed, i.e., the time-averaged lift coefficient $\overline{C_{\mathrm{L}}}$ has its maximum value at an appropriate value of $N_{\mathrm{K}}$, and $\overline{C_{\mathrm{L}}}$ decreases as $N_{\mathrm{K}}$ decreases.

Figure 10 shows the time variations of $\theta_{\mathrm{w}}$ and the trajectories of the center of the body for case (ii). We can see from Fig. 10(a) that the curves of $\theta_{\mathrm{w}}$ are quite similar to the results shown in Fig. 3 which was obtained when the body of the model is fixed, and the deviations in their amplitude are smaller than those in Fig. 9(a). This is because in case (ii) the nondimensional total mass $N_{\mathrm{M}}$ is large compared with case (i), and consequently the acceleration of the body motion is small. Actually, the vertical oscillations of the body motion during one period is not observed in Fig. 10(b). We can see from

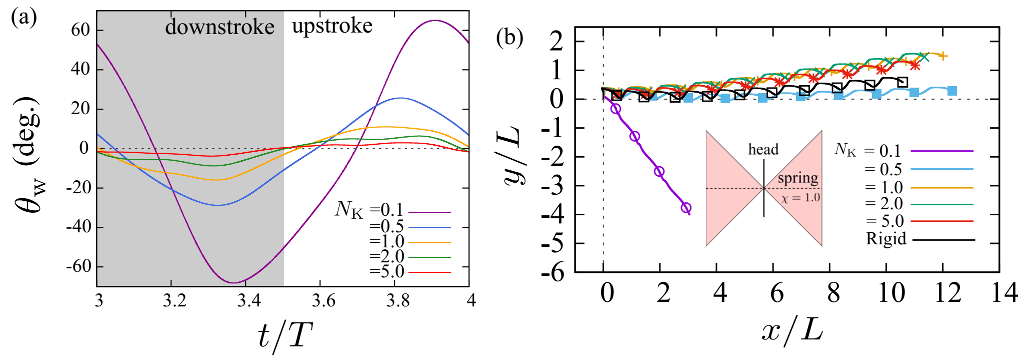

FIG. 9. (a) Time variations of the deflection angle $\theta_w$ and (b) trajectories of the center of the body for various values of the nondimensional spring stiffness $N_K$ in the free flights without rotation when $\chi = 1.0$, Re $= 1000$, and the other governing parameters are given as Set 1 in Table II.

Fig. 10(b) that the butterfly model can go forward and upward against gravity for any value of $N_K$, and the trajectory reaches the most upward position when $N_K = 5.0$. This suggests that the model can fly most effectively when $N_K = 5.0$ for case (ii). Although the most effective $N_K$ is slightly different from the value suggested in Fig. 7 (around $N_K = 1.0$ when Re $= 500$) presumably due to the increase in the forward speed, this result is also consistent with the results obtained when the body is fixed.

From the above results, we can see that the chordwise wing flexibility can improve the lift and thrust forces even in the free flight without rotation. However, the improvement due to the chordwise wing flexibility is not so large compared with the results for the rigid wings.

### *2. With pitching rotation*

Next, we simulate free flights of the butterfly model with rotation (pitching motion), i.e., we solve Eqs. (9)–(12) fully. Therefore, the model can rotate in the pitching direction, while it does not rotate in the yawing and rolling directions. The aim of this simulation is to investigate the effect of chordwise wing flexibility on the pitching motion of the model in addition to the translational motion. In this simulation, we consider the two cases (i) and (ii) shown in the previous section. The nondimensional moment of inertia of the body $N_I = I_b/(\rho_f L^5) =$ WR $\times N_M/12$ is equal to 0.252 and 5.06 for cases (i) and (ii), respectively. Unfortunately, we could not find available data of $I_b$ for actual insects. Therefore, we also check the effect of $I_b$.

Figure 11 shows the trajectories of the center of the body and the time variations of the pitching angle $\theta_p$ for case (i). We can see from this figure that neither the rigid wings nor the flexible wings can go upward against gravity. It should be noted that the butterfly model could go upward when the pitching motion is neglected as shown in Fig. 9(b). Therefore, the lift force decreases due to the pitching motion. Actually, the amplitude of the pitching angle $\theta_p$ during each period is about 60° as shown in Fig 11(b), and consequently the effective angle of attack $\theta_p + \alpha$ is likely to change. The effective AOA determines the directions of downstroke and upstroke and significantly affects the lift and thrust forces. Therefore, the model cannot obtain enough lift force supporting its weight when the pitching motion is considered due to the change of the effective AOA. In addition, for the flexible wings, $\theta_p$ increases averagely and eventually exceeds 90°. This means that the model with the flexible

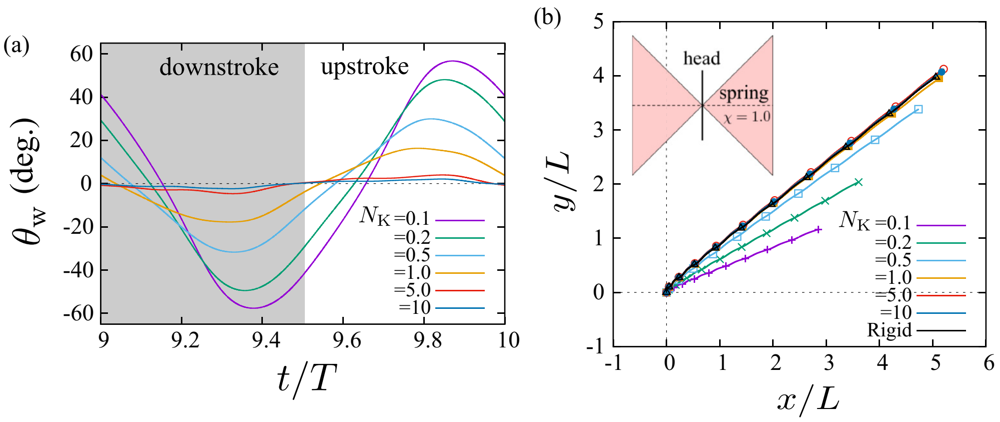

FIG. 10. (a) Time variations of the deflection angle $\theta_w$ and (b) trajectories of the center of the body for various values of the nondimensional spring stiffness $N_K$ in the free flights without rotation when $\chi = 1.0$, Re $= 500$, and the other governing parameters are given as Set 2 in Table II.

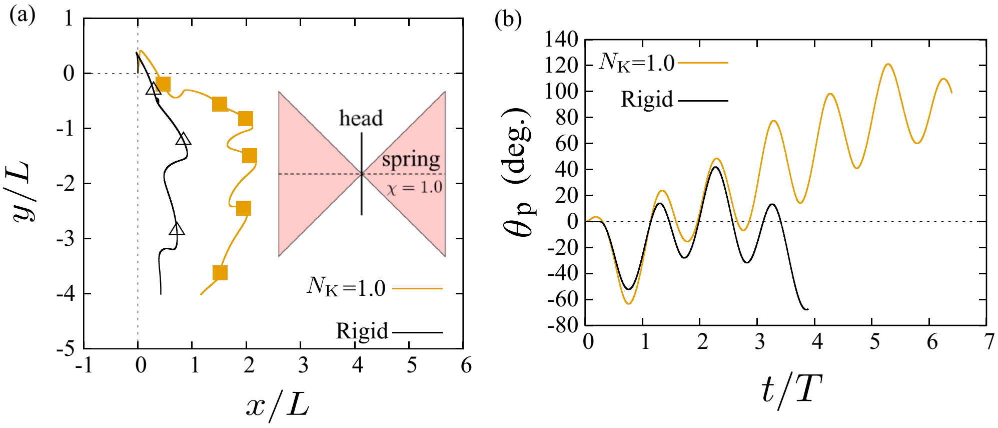

FIG. 11. (a) Trajectories of the center of the body and (b) time variations of the pitching angle $\theta_p$ for the flexible wings with the nondimensional spring stiffness $N_K$ equal to 1.0 and the rigid wings in the free flights with pitching rotation when $\chi = 1.0$, Re = 1000, and the other governing parameters are given as Set 1 in Table II.

wings can get off balance. The similar behavior was observed in the free flight of the present model with square rigid wings [12]. Although the model with the flexible wings can reduce the speed of falling as shown in Fig. 11(a), this is not because the pitching motion is stabilized but because the lift force is enhanced by the chordwise wing flexibility. Therefore, we cannot expect that the chordwise wing flexibility contributes to the passive control of the pitching motion.

Figure 12 shows the trajectories of the center of the body and the time variations of $\theta_p$ for case (ii). We can see from this figure that although the model can go forward and upward against gravity for any value of $N_K$ as well as for the rigid wings, $\theta_p$ gradually increases and eventually the model gets off balance. This result is consistent with that for case (i) in terms of the fact that the model cannot maintain its attitude stably. The trajectories and the time variations of $\theta_p$ significantly depend on the value of $N_K$. However, we cannot completely say that the chordwise wing flexibility can stabilize the free flight of the present model. For example, the model for $N_K = 1.0$ can stay closer to the horizontal trajectory without control as shown in Fig. 12(a). This is because the model largely lowers its head at the early stage and then raises its head gradually as shown in Fig. 12(b). However, the increase of $\theta_p$ cannot be stopped and eventually $\theta_p$ exceeds 90°. This suggests that there is no mechanism that can keep the value of $\theta_p$ in a favorable range. Therefore, we conclude again that it cannot be expected that the chordwise wing flexibility contributes to the passive control of the pitching motion.

The above conclusion is valid even when the value of the moment of inertia of the body $I_b$ is changed. We denote the value of $I_b$ used in Fig. 12 by $I_{b0}$. Figure 13 shows the trajectories of the center of the body and the time variations of $\theta_p$ when $I_b = 0.1I_{b0}$, $0.5I_{b0}$, $1.0I_{b0}$ (the same value used in Fig. 12), $2.0I_{b0}$, and $\infty$ (without rotation). We can see that although the model can go forward and upward against gravity for any value of $I_b$, $\theta_p$ gradually increases, and eventually the model gets off balance except for $I_b \geqslant 2.0I_{b0}$. When $I_b = 2.0I_{b0}$, the model seems to keep its attitude during $t/T \leqslant 16$. However, $\theta_p$ tends to increase at $t/T = 16$, and it is predicted that the model gets off balance in the same way as the results

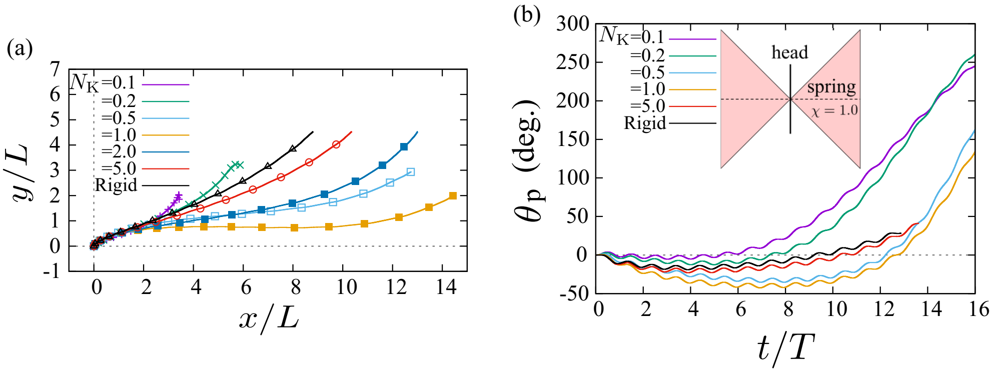

FIG. 12. (a) Trajectories of the center of the body and (b) time variations of the pitching angle $\theta_p$ for various values of the nondimensional spring stiffness $N_K$ in the free flights with pitching rotation when $\chi = 1.0$, Re = 500, and the other governing parameters are given as Set 2 in Table II.

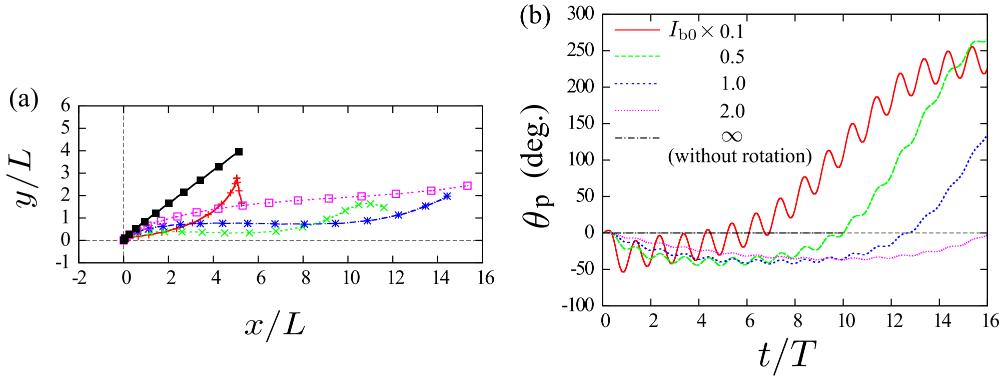

FIG. 13. (a) Trajectories of the center of the body and (b) time variations of the pitching angle $\theta_p$ for various values of the moment of inertia of the body $I_b$ in the free flights with pitching rotation when $N_K = 1.0$, $\chi = 1.0$, Re = 500, and the other governing parameters are given as Set 2 in Table II.

for other values of $I_b$. Therefore, even when we use different values of $I_b$, the chordwise wing flexibility cannot passively stabilize the free flight of the present model.

For the hovering wing kinematics of a fruit fly, it was suggested that insects may passively stabilize their hover flight via chordwise wing flexibility [36]. This seems to contradict to the present results. This is attributed to the differences in the wing kinematics and in the flight mode. Bluman *et al.* [36] focused on the wing kinematics inspired by a fruit fly and considered its hovering flight, i.e., a fixed-point equilibrium where the body is at rest due to the balance of gravitational force and torque, aerodynamic force and torque, and inertial force and torque. On the other hand, we focused on the wing kinematics idealized from those of butterflies, and considered starting from the resting state and the transitional motion to forward flight, i.e., the acceleration of the body motion is significant. The present conclusion that the passive control of the pitching motion by the chordwise wing flexibility cannot be expected suggests the difficulty in stably maintaining the attitude of the present model without active control. This might be related to the erratic flight behavior of butterflies.

## VI. CONCLUSIONS

We have investigated the effect of chordwise wing flexibility on the flapping flight of a simple butterfly model with numerical simulations based on the immersed boundary-lattice Boltzmann method. The model is composed of two triangle wings and a rod-shaped rigid body, and each wing is composed of two rigid plates connected by a torsion spring. The fore parts of the wings are flapped downward and backward in downstroke and upstroke, respectively, in a prescribed manner, whereas the hind parts move passively by the inertial, elastic, and aerodynamic forces. In the present study, we investigated the effect of chordwise wing flexibility on aerodynamic performance in terms of the nondimensional spring stiffness $N_K$ and the nondimensional length of the hind part $\chi$.

First, we investigated the effects of $N_K$ and $\chi$ on aerodynamic performance when the body of the model is fixed. We found that the time-averaged lift and thrust forces and the required power increase with $N_K$, and there is an appropriate range of $N_K$ where the time-averaged lift and thrust forces are larger than those for the rigid wings. The mechanism of the lift and thrust enhancements was considered that in the downstroke the flexible wings can generate not only the lift force but also the thrust force due to the deformation of the wings, and in the upstroke the thrust force can be generated in the same way. In addition, we found that the effect of chordwise wing flexibility decreases as $\chi$ decreases, since a small value of $\chi$ makes the area of the hind parts small. The tendency of the aerodynamic performance for $N_K$ was not so dependent on the Reynolds number Re and the other governing parameters.

Second, we simulated free flights when the body of the model can only move translationally. We found that the model with the flexible wings at an appropriate value of $N_K$ can fly more effectively than the model with the rigid wings, which is consistent with the results obtained when the body of the model is fixed.

Finally, we simulated free flights with pitching rotation. We found that the model gets off balance for any value of $N_K$. Therefore, we could not expect that the chordwise wing flexibility contributes to the passive control of the pitching motion.

## ACKNOWLEDGMENT

This work was supported by JSPS KAKENHI Grant No. JP16K18012.

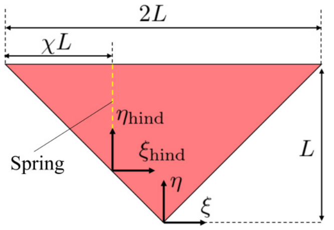

FIG. 14. The coordinate systems ($\xi$, $\eta$) and ($\xi_{\rm hind}$, $\eta_{\rm hind}$) fixed to the fore and hind parts, respectively, where $L$ is the wing length and $\chi$ is the nondimensional hind wing-tip length.

## APPENDIX A: DETAILED FORMS OF LAGRANGIANS

In this section we show the detailed forms of the Lagrangians shown in Sec. III B. The formulation is based on the coordinate systems $(\xi, \eta)$ and $(\xi_{\rm hind}, \eta_{\rm hind})$ fixed to the fore and hind parts, respectively, as shown in Fig. 14. The origin of $(\xi_{\rm hind}, \eta_{\rm hind})$ is located at the point $(1-\chi)L\,(-1, 1)$ observed in $(\xi, \eta)$.

The Lagrangian $\mathcal{L}_{\rm body}$ of the body is given by

$$\mathcal{L}_{\rm body} = \tfrac{1}{2}m_{\rm b}\big(\dot{x}_{\rm b}^2 + \dot{y}_{\rm b}^2\big) + \tfrac{1}{2}I_{\rm b}\dot{\theta}_{\rm p}^2 - m_{\rm b}Gy_{\rm b}, \tag{A1}$$

where the dot notation denotes the time derivative.

The Lagrangian $\mathcal{L}_{\rm fore}$ of the right fore part is given by

$$\begin{aligned}\mathcal{L}_{\rm fore} = {}& \tfrac{1}{4}m_{\rm w}^{\rm fore}(\dot{x}_{\rm b}^2 + \dot{y}_{\rm b}^2) + \tfrac{1}{2}m_{\rm w}^{\rm fore}S_{\xi\eta}^{\rm fore}(\dot{\theta}_{\rm p} + \dot{\alpha})\dot{\theta}\cos\theta + \tfrac{1}{4}m_{\rm w}^{\rm fore}S_{\xi\xi}^{\rm fore}(\dot{\theta}_{\rm p} + \dot{\alpha})^2 + \tfrac{1}{4}m_{\rm w}^{\rm fore}S_{\eta\eta}^{\rm fore}\{(\dot{\theta}_{\rm p} + \dot{\alpha})^2\sin^2\theta + \dot{\theta}^2\}\\ &+ \tfrac{1}{2}m_{\rm w}^{\rm fore}R_{\xi}^{\rm fore}(\dot{\theta}_{\rm p} + \dot{\alpha})\{-\dot{x}_{\rm b}\sin(\theta_{\rm p} + \alpha) + \dot{y}_{\rm b}\cos(\theta_{\rm p} + \alpha)\} - \tfrac{1}{2}m_{\rm w}^{\rm fore}R_{\eta}^{\rm fore}(\dot{\theta}_{\rm p} + \dot{\alpha})\sin\theta\{\dot{x}_{\rm b}\cos(\theta_{\rm p} + \alpha) + \dot{y}_{\rm b}\sin(\theta_{\rm p} + \alpha)\}\\ &+ \tfrac{1}{2}m_{\rm w}^{\rm fore}R_{\eta}^{\rm fore}\dot{\theta}\cos\theta\{-\dot{x}_{\rm b}\sin(\theta_{\rm p} + \alpha) + \dot{y}_{\rm b}\cos(\theta_{\rm p} + \alpha)\} - \tfrac{1}{2}m_{\rm w}^{\rm fore}G\big\{y_{\rm b} + R_{\xi}^{\rm fore}\sin(\theta_{\rm p} + \alpha) + R_{\eta}^{\rm fore}\cos(\theta_{\rm p} + \alpha)\sin\theta\big\},\end{aligned} \tag{A2}$$

where $m_{\rm w}^{\rm fore}$ is the total mass of the left and right fore parts, the vector $(R_{\xi}^{\rm fore}, R_{\eta}^{\rm fore})$ corresponds to the position of the center of mass of the right fore part observed in the coordinate $(\xi, \eta)$, and the matrix $S_{ij}^{\rm fore}$ $(i, j = \xi, \eta)$ corresponds to the inertia tensor of the right fore part divided by $m_{\rm w}^{\rm fore}/2$. These parameters are given by the total mass $m_{\rm w}$ of the left and right wings, the nondimensional hind wing-tip length $\chi$, and the wing length $L$ as follows:

$$m_{\rm w}^{\rm fore} = \left(1 - \frac{1}{2}\chi^2\right)m_{\rm w}, \tag{A3}$$

$$R_{\xi}^{\rm fore} = \frac{(3-2\chi)\chi^2}{3(2-\chi^2)}L, \tag{A4}$$

$$R_{\eta}^{\rm fore} = \frac{(2-\chi)^2(1+\chi)}{3(2-\chi^2)}L, \tag{A5}$$

$$S_{\xi\xi}^{\rm fore} = \frac{2 - 6\chi^2 + 8\chi^3 - 3\chi^4}{6(2-\chi^2)}L^2, \tag{A6}$$

$$S_{\xi\eta}^{\rm fore} = \frac{(2-\chi)^2\chi^2}{4(2-\chi^2)}L^2, \tag{A7}$$

$$S_{\eta\eta}^{\rm fore} = \frac{6 - 6\chi^2 + 4\chi^3 - \chi^4}{6(2-\chi^2)}L^2. \tag{A8}$$

The Lagrangian $\mathcal{L}_{\rm hind}$ of the right hind part is given by

$$\begin{aligned}\mathcal{L}_{\rm hind} = {}& \tfrac{1}{4}m_{\rm w}^{\rm hind}(\dot{x}_{\rm b}^2 + \dot{y}_{\rm b}^2) + \tfrac{1}{2}m_{\rm w}^{\rm hind}(1-\chi)L\{\dot{x}_{\rm b}(\dot{\phi}\sin\phi - \dot{\phi}\cos\phi\sin\theta - \dot{\theta}\sin\phi\cos\theta)\\ &+ \dot{y}_{\rm b}(-\dot{\phi}\cos\phi - \dot{\phi}\sin\phi\sin\theta + \dot{\theta}\cos\phi\cos\theta)\} + \tfrac{1}{4}m_{\rm w}^{\rm hind}(1-\chi)^2L^2\{\dot{\phi}^2(1+\sin^2\theta) + \dot{\theta}^2 - 2\dot{\phi}\dot{\theta}\cos\theta\}\\ &+ \tfrac{1}{2}m_{\rm w}^{\rm hind}S_{\xi\eta}^{\rm hind}(\dot{\phi}^2\sin\theta\cos\theta\sin\theta_{\rm w} + \dot{\phi}\dot{\theta}\cos\theta\cos\theta_{\rm w} + \dot{\phi}\dot{\theta}_{\rm w}\sin\theta\sin\theta_{\rm w} + \dot{\theta}\dot{\theta}_{\rm w}\cos\theta_{\rm w})\\ &+ \tfrac{1}{4}m_{\rm w}^{\rm hind}S_{\xi\xi}^{\rm hind}\{\dot{\phi}^2(\cos^2\theta_{\rm w} + \cos^2\theta\sin^2\theta_{\rm w}) + \dot{\theta}^2\sin^2\theta_{\rm w} + \dot{\theta}_{\rm w}^2 - 2\dot{\phi}\dot{\theta}\sin\theta\sin\theta_{\rm w}\cos\theta_{\rm w} + 2\dot{\phi}\dot{\theta}_{\rm w}\cos\theta\}\\ &+ \tfrac{1}{4}m_{\rm w}^{\rm hind}S_{\eta\eta}^{\rm hind}(\dot{\phi}^2\sin^2\theta + \dot{\theta}^2) + \tfrac{1}{2}m_{\rm w}^{\rm hind}R_{\xi}^{\rm hind}\{\dot{x}_{\rm b}(-\dot{\phi}\sin\phi\cos\theta_{\rm w} - \dot{\phi}\cos\phi\cos\theta\sin\theta_{\rm w} + \dot{\theta}\sin\phi\sin\theta\sin\theta_{\rm w}\\ &- \dot{\theta}_{\rm w}\cos\phi\cos\theta_{\rm w} - \dot{\theta}_{\rm w}\sin\phi\cos\theta\cos\theta_{\rm w}) + \dot{y}_{\rm b}(\dot{\phi}\cos\phi\cos\theta_{\rm w} - \dot{\phi}\sin\phi\cos\theta\sin\theta_{\rm w} - \dot{\theta}\cos\phi\sin\theta\sin\theta_{\rm w}\\ &- \dot{\theta}_{\rm w}\sin\phi\sin\theta_{\rm w} + \dot{\theta}_{\rm w}\cos\phi\cos\theta\cos\theta_{\rm w}) + (1-\chi)L(-\dot{\phi}^2\cos\theta_{\rm w} + \dot{\phi}^2\sin\theta\cos\theta\sin\theta_{\rm w} + \dot{\phi}\dot{\theta}\sin\theta\sin\theta_{\rm w}\\ &+ \dot{\phi}\dot{\theta}\cos\theta\cos\theta_{\rm w} - \dot{\phi}\dot{\theta}_{\rm w}\cos\theta\cos\theta_{\rm w} + \dot{\phi}\dot{\theta}_{\rm w}\sin\theta\sin\theta_{\rm w} + \dot{\theta}\dot{\theta}_{\rm w}\cos\theta_{\rm w})\}\\ &+ \tfrac{1}{2}m_{\rm w}^{\rm hind}R_{\eta}^{\rm hind}\{-\dot{x}_{\rm b}(\dot{\phi}\cos\phi\sin\theta + \dot{\theta}\sin\phi\cos\theta) + \dot{y}_{\rm b}(-\dot{\phi}\sin\phi\sin\theta_{\rm w} + \dot{\theta}\cos\phi\cos\theta)\\ &+ (1-\chi)L(\dot{\phi}^2\sin^2\theta - \dot{\phi}\dot{\theta}\cos\theta + \dot{\theta}^2)\}\\ &- \tfrac{1}{2}m_{\rm w}^{\rm hind}G\big\{y_{\rm b} + (1-\chi)L(-\sin\phi + \cos\phi\sin\theta) + R_{\xi}^{\rm hind}(\sin\phi\cos\theta_{\rm w} + \cos\phi\cos\theta\sin\theta_{\rm w}) + R_{\eta}^{\rm hind}\cos\phi\sin\theta\big\}\\ &-\tfrac{1}{2}K\theta_{\rm w}^2,\end{aligned} \tag{A9}$$

where $\phi$ is the effective angle of attack given by $\theta_{\rm p} + \alpha$, $m_{\rm w}^{\rm hind}$ is the total mass of the left and right hind parts, the vector $(R_{\xi}^{\rm hind}, R_{\eta}^{\rm hind})$ corresponds to the position of the center of mass of the right hind part observed in the coordinate $(\xi_{\rm hind}, \eta_{\rm hind})$, and the matrix $S_{ij}^{\rm hind}$ $(i, j = \xi, \eta)$ corresponds to the inertia tensor of the right hind part divided by $m_{\rm w}^{\rm hind}/2$.

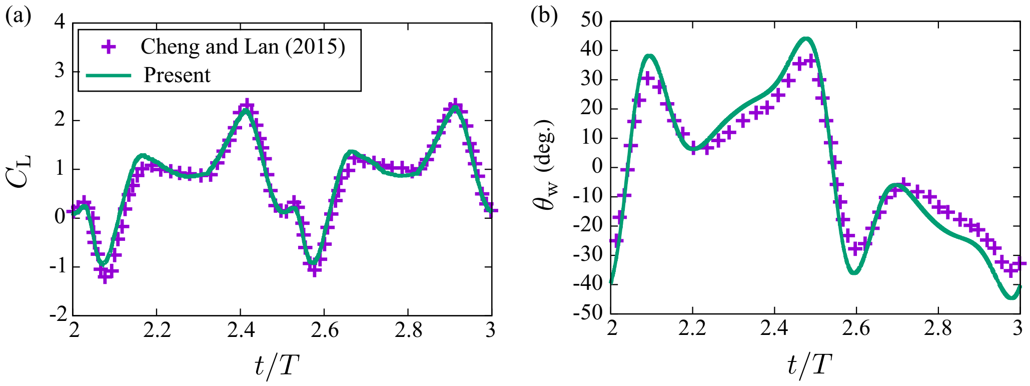

FIG. 15. Time variations of (a) the lift coefficient $C_L$ and (b) the deflection angle $\theta_w$ for the flexible wing with $K^* = 5$ during the third period when Re = 200, $\Phi = 150^\circ$, $\Psi = 0^\circ$, and $\alpha_m = 35^\circ$.

These parameters are given by the total mass $m_w$ of the left and right wings, the nondimensional hind wing-tip length $\chi$, and the wing length $L$ as follows:

$$m_w^{\text{hind}} = \tfrac{1}{2}\chi^2 m_w, \tag{A10}$$

$$R_\xi^{\text{hind}} = -\tfrac{1}{3}\chi L, \tag{A11}$$

$$R_\eta^{\text{hind}} = \tfrac{2}{3}\chi L, \tag{A12}$$

$$S_{\xi\xi}^{\text{hind}} = \tfrac{1}{6}\chi^2 L^2, \tag{A13}$$

$$S_{\xi\eta}^{\text{hind}} = -\tfrac{1}{4}\chi^2 L^2, \tag{A14}$$

$$S_{\eta\eta}^{\text{hind}} = \tfrac{1}{2}\chi^2 L^2. \tag{A15}$$

### APPENDIX B: VALIDATION FOR A FLEXIBLE WING

In order to validate the present numerical method for the flexible wing, we calculate a flow around a flapping wing with chordwise flexibility, which was simulated by Cheng and Lan [10] using the artificial compressibility method with the body-conforming grid [37]. The wing used in this simulation is a rectangular flat plate with chord length $c$ and wing length $R = 3c$. The wing is composed of the leading and aft portions connected by a torsion spring. The chord length and wing length of the leading portion are $0.5c$ and $R$, respectively, and those of the aft portion are the same. The motion of the leading portion is prescribed by the simplified wing kinematics of fruit fly [38]. The mathematical formulation of this motion is shown in Refs. [10,37]. This motion is governed by the three kinematic parameters, i.e., stroke amplitude $\Phi$, phase difference $\Psi$, and angle of attack at midstroke $\alpha_m$. In this simulation, we set $\Phi = 150^\circ$, $\Psi = 0^\circ$, and $\alpha_m = 35^\circ$. The aft portion responds passively due to its mass $m_2$ and the spring stiffness $K$ of the torsion spring. The deflection angle of the aft portion is denoted by $\theta_w$. The equation of $\theta_w$ is shown in Ref. [10].

The characteristic length is taken as the chord length $c$, and the characteristic speed is taken as $U_{\text{ref}} = 2\Phi r_2/T$, where $r_2$ is the radius of the second moment of wing area and is equal to $0.56R$, and $T$ is the period of wing beat cycle. The governing parameters of the system are the Reynolds number $\text{Re} = cU_{\text{ref}}/\nu$, the nondimensional mass of the aft portion $m^* = m_2/(\rho_f c^3)$, and the nondimensional spring stiffness $K^* = K/(\rho_f c^5/T^2)$. In this simulation, we set Re = 200, $m^* = 0.96$, and $K^* = 5$.

In the simulation by the IB-LBM, we set the $x$-$y$ plane to be parallel to the stroke plane and the $z$ axis to point upward. We use a computational domain with $[-2L, 2L] \times [-2L, 2L] \times [0, 8L]$, and the position of the wing root is set at $(0, 0.28L, 6.4L)$. As for the boundary condition of the domain, a no-slip boundary condition is used on all sides of the domain. We use a multiblock grid [31] composed of a fine grid with $\Delta x$ in $[-1.5L, 1.5L] \times [-1.5L, 1.5L] \times [5.6L, 7.2L]$ and a coarse grid with $2\Delta x$ in the other domain. We represent the wing by an arrangement of boundary Lagrangian points on an infinitely thin plate, i.e., the wing has effective thickness but converges to a thin object with no volume in the limit $\Delta x \to 0$, whereas in the simulation by Cheng and Lan [10] the wing had a finite thickness equal to $0.03c$. In this simulation, we set $c = 40\Delta x$ and $T = 18000\Delta t$.

We calculate the lift coefficient $C_L = F_z/(0.5\rho_f U_{\text{tip}}^2 Lc)$ (where $F_z$ is the aerodynamic force in the $z$ direction) and the deflection angle $\theta_w$. Figure 15 shows the time variations of $C_L$ and $\theta_w$ in $2 \leqslant t/T \leqslant 3$. The results obtained with the present method agree well with the numerical results computed by Cheng and Lan [10].

[1] C. P. Ellington, J. Exp. Biol. **202**, 3439 (1999).

[2] K. Y. Ma, P. Chirarattananon, S. B. Fuller, and R. J. Wood, Science **340**, 603 (2013).

[3] L. Ristroph and S. Childress, J. R. Soc. Interface **11**, 20130992 (2014).

[4] W. Shyy, Y. Lian, J. Tang, D. Vieiru, and H. Liu, *Aerodynamics of Low Reynolds Number Flyers* (Cambridge University Press, New York, 2008).

[5] L. Zhao, Q. Huang, X. Deng, and S. P. Sane, J. R. Soc. Interface **7**, 485 (2010).

[6] L. Zheng, T. Hedrick, and R. Mittal, Bioinspir. Biomim. **8**, 036001 (2013).

[7] T. Nakata and H. Liu, J. Comput. Phys. **231**, 1822 (2012).

[8] S. A. Combes and T. L. Daniel, J. Exp. Biol. **206**, 2979 (2003).

[9] J. D. Eldredge, J. Toomey, and A. Medina, J. Fluid Mech. **659**, 94 (2010).

[10] X. Cheng and S. Lan, J. Bionic Eng. **12**, 432 (2015).

[11] A. Medina, J. D. Eldredge, J. Kweon, and H. Choi, AIAA J. **53**, 2607 (2015).

[12] K. Suzuki, K. Minami, and T. Inamuro, J. Fluid Mech. **767**, 659 (2015).

[13] Y.-H. J. Fei and J.-T. Yang, Phys. Rev. E **92**, 033004 (2015).

[14] Y.-H. J. Fei and J.-T. Yang, Phys. Rev. E **93**, 033124 (2016).

[15] N. Yokoyama, K. Senda, M. Iima, and N. Hirai, Phys. Fluids **25**, 021902 (2013).

[16] M. Fuchiwaki and K. Tanaka, Trans. JSME (in Japanese) **82**, 15-00425 (2016).

[17] L. Ristroph, A. J. Bergou, J. Guckenheimer, Z. J. Wang, and I. Cohen, Phys. Rev. Lett. **106**, 178103 (2011).

[18] S. K. Jones, R. Laurenza, T. L. Hedrick, B. E. Griffith, and L. A. Miller, J. Theor. Biol. **384**, 105 (2015).

[19] C. P. Ellington, Philos. Trans. R. Soc. Lond. B **305**, 79 (1984).

[20] K. Suzuki and M. Yoshino, Fluid Dyn. Res. **49**, 035512 (2017).

[21] K. Suzuki and M. Yoshino, Commun. Comput. Phys. **23**, 951 (2018).

[22] K. Suzuki, I. Okada, and M. Yoshino (unpublished).

[23] K. Suzuki and T. Inamuro, Comput. Fluids **49**, 173 (2011).

[24] S. Sunada, K. Kawachi, I. Watanabe, and A. Azuma, J. Exp. Biol. **183**, 249 (1993).

[25] G. Bimbard, D. Kolomenskiy, O. Bouteleux, J. Casas, and R. Godoy-Diana, J. Exp. Biol. **216**, 3551 (2013).

[26] C.-K. Kang, J. Cranford, M. K. Sridhar, D. Kodali, and D. B. Landrum, AIAA J. **56**, 15 (2018).

[27] A. O. Ancel, R. Eastwood, D. Vogt, C. Ithier, M. Smith, R. Wood, and M. Kovač, Interface Focus **7**, 20160087 (2017).

[28] D. J. Acheson, *Elementary Fluid Dynamics* (Oxford University Press, Oxford, 1990).

[29] K. Suzuki, I. Okada, and M. Yoshino, J. Fluid Sci. Technol. **11**, JFST0017 (2016).

[30] T. Engels, D. Kolomenskiy, K. Schneider, and J. Sesterhenn, SIAM J. Sci. Comput. **38**, S3 (2016).

[31] T. Inamuro, Fluid Dyn. Res. **44**, 024001 (2012).

[32] R. Dudley, J. Exp. Biol. **150**, 37 (1990).

[33] J. C. R. Hunt, A. A. Wray, and P. Moin, Proceedings of the Summer Program, 1988, p. 193, https://ntrs.nasa.gov/archive/nasa/casi.ntrs.nasa.gov/19890015184.pdf.

[34] M. Vanella, T. Fitzgerald, S. Preidikman, E. Balaras, and B. Balachandran, J. Exp. Biol. **212**, 95 (2009).

[35] S. A. Combes and T. L. Daniel, J. Exp. Biol. **206**, 2999 (2003).

[36] J. E. Bluman, M. K. Sridhar, and C.-K. Kang, J. R. Soc. Interface **15**, 20180409 (2018).

[37] M. Sun and J. Tang, J. Exp. Biol. **205**, 55 (2002).

[38] M. H. Dickinson, F. O. Lehmann, and S. P. Sane, Science **284**, 1954 (1999).